Available online at www.sciencedirect.com
ScienceDirect
Lithos 96 (2007) 543–566
LITHOS
www.elsevier.com/locate/lithos

Petrogenesis of the Early Jurassic Nandaling flood basalts in the Yanshan belt, North China Craton: A correlation between magmatic underplating and lithospheric thinning

Zhihong Wang [a,*], Yue Zhao [b], Haibo Zou [c], Wuping Li [d], Xiaowen Liu [e], Hai Wu [e], Gang Xu [b], Suanhong Zhang [b]

[a] State Key Laboratory of Lithospheric Evolution, Institute of Geology and Geophysics, Chinese Academy of Sciences, Beijing, 100029, China
[b] Institute of Geomechanics, Chinese Academy of Geological Sciences, Beijing, 100081, China
[c] Department of Earth and Space Sciences, University of California at Los Angeles, Los Angeles, CA 90095, USA
[d] Guangzhou Institute of Geochemistry, Chinese Academy of Sciences, Guangzhou, 510640, China
[e] Centre of Geological Materials, The Ministry of Land and Resources P.R.C., Hebei, 065201, China

Received 7 November 2005; accepted 4 December 2006
Available online 19 December 2006

Abstract

Integrated geochemical and Sr–Nd–Pb isotopic studies of the Early Jurassic Nandaling flood basalts (NFB) in the Yanshan belt, northern margin of the North China Craton (NCC), are presented in this paper. These sub-alkaline basalts evolved from a more magnesium-rich parental magma through fractional crystallization of olivine and clinopyroxene. The primitive magma of the NFB originated from 2–5% partial melting of spinel to garnet transitional peridotite at about 70–80 km depth in the Mesozoic lithosphere mantle. The NFB contain a distinctive lithospheric component, characterized by Nb (Ta), Th, U and Ti depletions, LREE enrichments, moderate Sr, and low Nd and Pb initial isotopic ratios, as a result of an interaction between lower crust (15–25%) and primitive magma evoked by magmatic underplating at crust–mantle boundary. The Early Jurassic NFB extruded in an intraplate extensional setting related to post-orogenic collapse in the northern margin of the NCC, indicating an event of lithospheric modification earlier than that in the southern margin (Early Cretaceous). The temporal similarity of the Jurassic–Cretaceous mantle-derived mafic rocks to lower crust replacement, and the decoupling of surface shortening with lithospheric thinning during the Late Jurassic–Early Cretaceous, suggest the important role of magmatic underplating and subsequent crust–mantle interaction accompanied by asthenosphere upwelling on the evolution of the Mesozoic lithosphere of the NCC. The correlation between lithospheric thinning and magmatic underplating may be an important process in continental rifting.
© 2007 Elsevier B.V. All rights reserved.

Keywords: Early Jurassic Nandaling flood basalts; Petrogenesis; Magmatic underplating; Lithospheric thinning; North China Craton

1. Introduction

The tremendous modification of the lithospheric mantle beneath the NCC, namely, from an old and cold cratonic lithospheric mantle to a Cenozoic oceanic-like lithospheric mantle, accompanied by about 120 km

* Corresponding author. Tel.: +86 010 62008129; fax: +86 010 62010846.
E-mail address: z-hwang@mail.iggcas.ac.cn (Z. Wang).

0024-4937/$ - see front matter © 2007 Elsevier B.V. All rights reserved.
doi:10.1016/j.lithos.2006.12.004

lithosphere loss, has attracted extensive attention from worldwide geologists (e.g., Griffin et al., 1992; Menzies et al., 1993; Griffin et al., 1998; Menzies and Xu, 1998; Fan et al., 2000; Xu, 2001; O'Reilly et al., 2001; Wilde et al., 2003). The interpretation for direct cause of significant lithospheric replacement was controversial, including thermal–mechanical–chemical erosion (e.g., Menzies and Xu, 1998; Xu, 2001), dispersion and dilution (e.g., Yuan, 1996; O'Reilly et al., 2001), delamination (e.g., Deng et al., 2000; Zhou et al., 2002), and interaction between slab-related melts and refractory lithosphere (Zhang et al., 2003). Various geodynamic mechanisms had been proposed, mostly with emphasis on distinctive circum-cratonic subduction and/or collision, such as Pacific Ocean subduction (Tatsumoto et al., 1992), Yangtze crust subduction and subsequent collision between the South and North China cratons (Xu, 2001; Zheng et al., 2001, 2003), Paleo-Asian Ocean and Mongol–Okhotsk Ocean subduction and suturing (Zhang et al., 2003). One of exceptional mechanisms was proposed by Wilde et al. (2003) who correlated the lithospheric thinning with the breakup and dispersal of Gondwanaland accompanied by a major mantle overturn. Accordingly, the proposed timing for the lithospheric replacement ranges from Proterozoic (e.g., Gao et al., 2002) to Cenozoic, but a Mesozoic time has been mostly favored (e.g., Xu, 2001; Wilde et al., 2003; Zhang et al., 2003).

The Jurassic–Cretaceous basaltic–andesitic volcanic rocks, occurred in several fault-related rift basins in the Yanshan belt, northern margin of the NCC (e.g., Chen et al., 1997; Davis et al., 2001a), offer a unique opportunity to probe the nature of underlying lithospheric mantle, to assess geodynamic models for the Mesozoic lithospheric modification, and to constrain magmatic and tectonic evolution of the Yanshan intraplate belt during the transitional process from the Paleo-Asian to Paleo-Pacific tectonic realms. Recent investigation of these rocks has

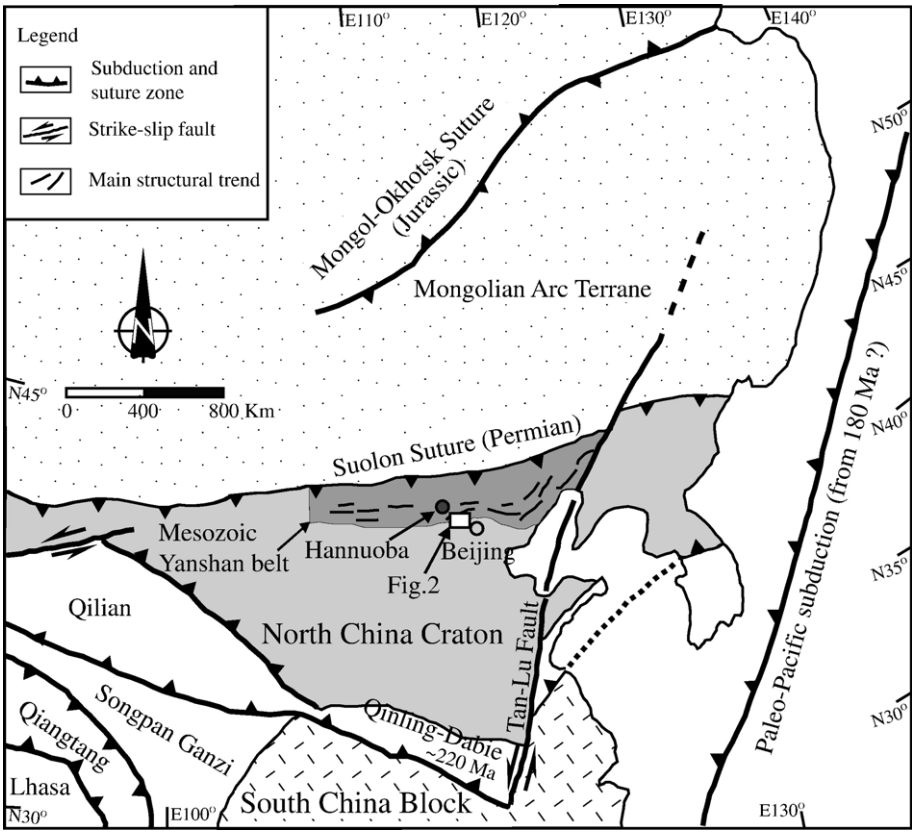


Fig. 1. Simplified regional tectonic map of eastern Asia with emphasis on the North China Craton (modified from Zheng et al., 2000; Ritts et al., 2001). The North China Craton collided with the South China block at ~220 Ma forming the Qiling–Dabie orogenic belt (e.g., Jahn et al., 1999), and with the Mongolian arc terranes in the Permian along the Suolon suture (e.g., Yin and Nie, 1996). The Mongol–Okhotsk Ocean between the amalgamated North China–Mongolian plate and the Siberian plate sutured during the Jurassic–Cretaceous (e.g., Zorin, 1999). The subduction of the Paleo-Pacific Ocean initiated at 180 Ma (e.g., Isozaki, 1997). The overall North China Craton including the Yanshan belt was definitely in an intraplate tectonic setting since the Triassic.

been mainly focused on the Cretaceous ones, and has reached some important results for the lithospheric thinning (e.g., Zhang et al., 2003). In contrast, studies of the Jurassic rocks lag far behind and are highly desirable.

Here we present detailed major- and trace-element geochemistry and Sr–Nd–Pb isotopes on the Early Jurassic Nandaling flood basalts in the Yanshan belt. The aims of this paper are to investigate the origin of the basalts and the nature of the lithospheric mantle beneath the NCC in the Mesozoic, and to provide constraints on the Mesozoic geodynamic evolution of the Yanshan belt and on the mechanism of lithospheric thinning of the NCC.

2. Geological background

2.1. Geological setting

The east–west striking Yanshan belt is located in the northern margin of the NCC (Fig. 1). To the north of the Yanshan belt are the Mongolian arc terranes. The Suolon suture marks the closure of the Paleo-Asian Ocean and the collision between the NCC and Mongolian composite terranes during the Permian (e.g., Yin and Nie, 1996; Badarch et al., 2002). To the south of the Yanshan belt are the Mesozoic–Cenozoic Ordos and Bohai Bay basins. The eastern edge of the Yanshan belt coincides with terminates at the Tanlu Fault.

The Yanshan belt is overlain by Archean rocks. A giant rift, namely, "Yan-Liao Rift", was developed in the belt roughly at 1.5–1.8 Ga, and is filled with volcanic and sedimentary rocks (Changcheng Formation). Cambrian–Mid Ordovician marine sediments (mainly carbonates) are widely distributed in the belt. From the Mid-Carboniferous to Lower Permian, there are alternating marine–terrestrial deposits overlain by terrestrial coal-bearing sediments. Upper Permian–Triassic unit comprises red bed, sandstone, and conglomerate as well as alluvial deposits, and some of them are molasses-type deposits associated with the aforementioned Permian collision. The Yanshan belt became an intraplate belt after the Permian collision, about 1000 km away from the subduction zones of the Mongol–Okhotsk and Paleo-Pacific Ocean (Fig. 1).

Jurassic–Cretaceous strata, consisting of terrestrial volcanic, volcanoclastic and clastic rocks, unconformably overlie the older sequences. These volcanic rocks, varying from mafic to intermediate-acid in compositions, were genetically related to the process of lithospheric replacement beneath the NCC (e.g., Zhang et al., 2003). The Jurassic–Cretaceous magmatism and tectonism were extensively regarded as imprints of the geodynamic transition from the Paleo-Asian to Paleo-Pacific tectonic realms and imprints of the fundamental lithospheric modification beneath the NCC.

2.2. A time sequence of tectonic events in the Yanshan belt

As shown in Fig. 1, subduction process adjacent to the NCC terminated at 220 Ma BP, and the two subduction zones in process, the Mongol–Okhotsk and

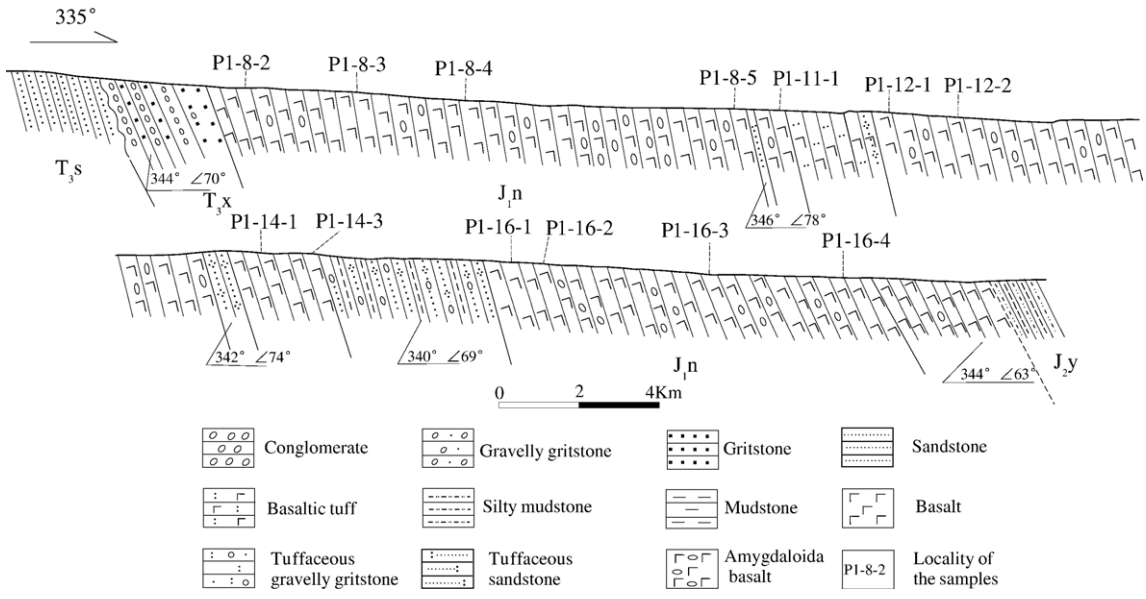


Fig. 2. The cross-section of the sampled NFB basalts in the Western Hills. T_3s — Late Triassic Shuangquan Formation, T_3x — Late Triassic Xingshikou Formation, J_1n — Early Jurassic Nandaling Formation, and J_2y — Middle Jurassic Yaopo Formation.

Paleo-Pacific oceans, respectively, were near 1000 km away from the NCC. There is no doubt that the overall NCC, including the Yanshan belt, had been in an intraplate setting since 220 Ma BP. Thus, any attempt to link the Jurassic–Cretaceous magmatism in the NCC directly to subduction processes is not convincing.

Based on field studies and radiometric dating, a pre-Middle Jurassic (>180 Ma) intensive tectonic event was recognized in the Yanshan belt (Davis et al., 1998; Zheng et al., 2000; Davis et al., 2001a). It is characterized by Archean basement-involved and south-dipping low-angle thrust faulting. As suggested by Davis et al. (2001a), this event was associated with the collision between the NCC and Mongolian arc terranes along the Suolon suture. The time of this event seems to be Permian–Triassic in age, identical to or slight later than the suturing time (Fig. 1).

The northern margin of the NCC was tectonically dominated by extension during the Triassic and Early Jurassic, based on the following observations: (1) the Triassic Xingshikou Formation in the study area is composed of molasses-type conglomerate and gritstone (Shao et al., 1997) (Fig. 2), indicating the erosion of the crust thickened by the aforementioned thrusting; (2) 208–250 Ma alkali igneous complexes, consisting mainly of nepheline syenites and A-type granites, are widely distributed in the Yanshan belt (Yan et al., 2000); and (3) a late Triassic metamorphic core complex was reported by Davis et al. (2001b) in the eastern Inner Mongolia, north of the Suolon suture.

In the Early Jurassic, a series of rift basins were developed on the amalgamated NCC and Mongolian plate, such as the Yingen basin (e.g., Jin et al., 2000; Meng, 2003), western Daqing Shan basin (Darby et al., 2001; Ritts et al., 2001), and Western Hills basin (e.g., Zhao et al., 2002). Most of the basins were bounded and controlled by normal faulting, and some normal faults were reversed from pre-existing thrust faults (e.g., Jin et al., 2000). All the basins are mainly filled with clastic sediments, while some basins, for example, the Western Hills Basin, are floored with flood basalts. The Nandaling flood basalts in the Western Hills Basin are the main focus of this paper.

The characteristics of the Triassic–Early Jurassic extensional activities are obviously consistent with progressive gravitational collapse of the Permian contractile orogenic belt constructed by the collision between the NCC and Mongolia arc terranes. This interpretation is supported by a temporal succession from the Permian to Early Jurassic, and a corresponding tectonic sequence from collision to shortening and to extension. Thus, it is clear that the Yanshan belt belonged to the Paleo-Asian realm in the sense of geodynamics at least prior to Early Jurassic. A long-distance effect from the Mongol–Okhotsk subduction during Early Jurassic could be possible, but is unnecessary and undocumented.

After the Early-Middle Jurassic extension and before the whole-scale extension in the Late Cretaceous, several stages of compressional deformation (mainly south- or north-ward thrusting) developed in the belt (about 160–120 Ma; e.g., Zheng et al., 2000; Davis et al., 2001a) during the Late Jurassic–Early Cretaceous times. The cause for this main north–south intraplate shortening may or may not be related to the Jurassic–Cretaceous collision of the amalgamated North China–Mongolian plate with the Siberian plate along the Mongol–Okhotsk suture zone, near 1000 km north of the Yanshan belt (e.g., Zhao et al., 1994; Zheng et al., 2000; Davis et al., 2001a).

2.3. The age, petrography and classification of the Nandaling flood basalts

The Nandaling flood basalts from the Western Hills near Beijing are underlain by conglomerate and gritstone of the Xingshikou Formation that bears Late Triassic fossil plants, and are overlain by the silty mudstone of the Mid-Jurassic Yaopo Formation that contains the fossils of *Coniopteris–Phoenicopsis* (Fig. 2). Although no fossil was found in the Nandaling Formation, multiple fossil plants with Early Jurassic age were observed from sediments interlayered with equivalent basalts from Chengde (Sun et al., 1996). A SHRIMP U–Pb zircon age of 197±6 Ma was recently obtained from the basalts (Zhao, unpublished data). Thus, the eruption age of the NFB was regarded as Early Jurassic, or 195–180 Ma (Zhao et al., 2002). The Nandaling flood basalts are

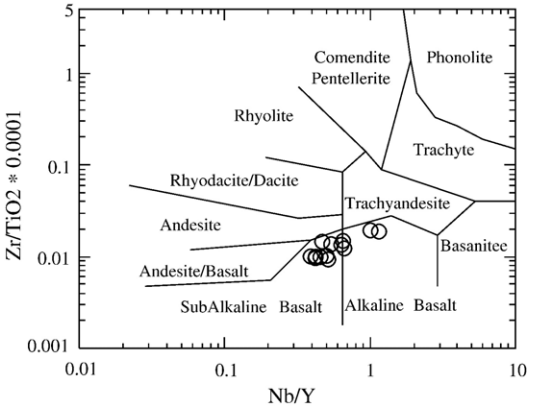


Fig. 3. Nb/Y vs. Zr/TiO_2 diagram for rock classification. The symbols for the NFB basalts (open circles) in subsequent figures are identical to those in Fig. 3.

Table 1
Major (wt.%) and trace element (ppm) compositions of the Nandaling flood basalts

Sample	P1-8-2	P1-8-3	P1-8-4	P1-8-5	P1-11-1	P1-12-1	P1-12-2	P1-14-1	P1-14-3	P1-16-1	P1-16-2	P1-16-3	P1-16-4
SiO_2	46.56	49	50.23	49.89	47.99	50.76	46.66	49.69	46.31	51.31	51.23	53	47.86
TiO_2	1.96	2	2.01	2.24	1.81	1.74	1.8	2.11	2.11	1.94	1.76	2	1.73
Al_2O_3	16.23	15.68	16.48	16.66	16.15	15.6	16.4	16.65	20.74	19.51	17.93	17.18	15.93
Fe_2O_3T	11.22	11.23	10.71	11.4	11.17	10.18	11.05	14.82	12.59	9.82	11.34	12.38	10.84
MnO	0.23	0.15	0.16	0.16	0.13	0.13	0.16	0.15	0.2	0.11	0.17	0.07	0.21
MgO	4.48	6.4	5.21	4.45	5.31	4.69	7.27	1.64	1.97	1.06	1.4	2.26	6.53
CaO	6.6	5.5	7.77	4.98	10.06	7.08	8.2	3.44	2.69	3.22	4.69	2.31	8.98
Na_2O	4.67	2.55	4.02	2.43	3.09	3.39	3.02	5.82	0.75	2.2	2.52	1.65	2.27
K_2O	0.2	2.95	0.83	3.75	0.68	2.77	1.64	2.84	8.42	6.76	5.55	5.68	0.48
P_2O_5	0.67	0.7	0.75	1.15	0.79	1.02	0.58	0.68	0.82	1.15	0.95	0.52	0.45
LOI	6.79	3.81	2.74	3.57	3.05	2.66	3.38	2.46	3.63	3.07	2.63	3.2	5.26
Total	99.61	99.96	100.91	100.69	100.21	100.03	100.16	100.3	100.22	100.14	100.18	100.26	100.54
Recalculated volatile-free oxide compositions													
SiO_2	49.97	50.94	51.63	51.72	49.5	52.15	48.29	50.94	48.05	52.93	52.61	54.75	50.5
TiO_2	2.1	2.08	2.07	2.32	1.87	1.79	1.86	2.16	2.19	2	1.81	2.07	1.83
Al_2O_3	17.42	16.3	16.94	17.27	16.66	16.03	16.97	17.07	21.52	20.13	18.41	17.75	16.81
Fe_2O_3T	12.04	11.67	11.01	11.82	11.52	10.46	11.44	15.19	13.06	10.13	11.65	12.79	11.44
MnO	0.25	0.16	0.16	0.17	0.13	0.13	0.17	0.15	0.21	0.11	0.17	0.07	0.22
MgO	4.81	6.65	5.36	4.61	5.48	4.82	7.52	1.68	2.04	1.09	1.44	2.33	6.89
CaO	7.08	5.72	7.99	5.16	10.38	7.27	8.49	3.53	2.79	3.32	4.82	2.39	9.48
Na_2O	5.01	2.65	4.13	2.52	3.19	3.48	3.13	5.97	0.78	2.27	2.59	1.7	2.4
K_2O	0.21	3.07	0.85	3.89	0.7	2.85	1.7	2.91	8.74	6.97	5.7	5.87	0.51
P_2O_5	0.72	0.73	0.77	1.19	0.81	1.05	0.6	0.7	0.85	1.19	0.98	0.54	0.47
Mg#	48	57	53	47	52	51	60	20	26	20	22	30	58
P	3028	3319	3404	5237	3381	4454	2599	2470	3494	4945	3962	2260	2044
Ti	13,141	13,977	13,372	15,079	11,018	10,377	11,165	10,162	12,508	11,620	10,025	11,801	10,586
V	182	189	183	158	170	177	195	139	129	182	128	100	186
Cr	170	172	107	12	79	186	217	313	195	148	149	278	276
Co	38	41	33	29	38	32	41	31	39	34	28	44	39
Ni	94	99	61	27	81	80	115	136	71	76	68	160	114
Rb	5	51	13	61	9	43	22	59	217	150	102	83	8
Sr	738	450	1192	525	2035	787	823	226	57	170	1375	50	1945
Y	32.8	33.2	34.6	35.7	28.1	29.2	26.6	31.6	34.3	30.1	30.1	25.8	25.5
Zr	276	184	267	227	245	271	191	200	276	365	345	197	178
Nb	15.38	16.96	18.61	13.93	17.64	19.17	11.21	13.12	23.03	34.57	30.31	11.87	12.87
Ba	321	1759	452	3110	408	2083	1357	1015	2304	2427	3061	6656	547
La	43.05	49.34	50.67	58.05	45.73	53.89	27.51	34.93	57.46	95.72	83.00	24.96	22.73
Ce	92.56	102.70	107.70	125.00	98.50	107.90	61.79	69.14	119.20	189.70	158.70	57.53	51.74
Pr	12.10	13.40	13.72	16.90	13.05	13.69	8.44	8.06	15.30	23.04	19.14	8.00	7.14
Nd	47.91	52.86	53.93	69.09	53.07	55.88	36.18	33.08	61.84	87.80	72.79	34.29	30.61
Sm	8.99	9.65	9.71	12.05	8.80	9.31	6.80	5.97	10.54	13.03	11.06	6.61	6.01
Eu	2.67	2.72	2.73	3.60	2.63	2.52	2.13	1.86	2.97	3.23	2.69	1.60	1.95
Gd	7.33	8.27	7.65	9.35	7.26	7.85	6.43	6.10	8.82	9.06	8.18	6.58	5.91
Tb	1.19	1.29	1.23	1.36	1.02	1.09	0.94	0.91	1.29	1.27	1.16	0.97	0.87
Dy	6.29	6.83	6.56	7.05	5.48	5.85	5.26	5.28	7.07	6.39	6.02	5.54	4.85
Ho	1.21	1.28	1.26	1.36	0.97	1.07	0.99	1.01	1.29	1.14	1.08	1.04	0.92
Er	3.11	3.11	3.22	3.51	2.86	3.06	2.83	3.04	3.75	3.25	3.18	3.06	2.64
Tm	0.48	0.44	0.49	0.53	0.40	0.44	0.40	0.44	0.54	0.44	0.45	0.44	0.38
Yb	2.85	2.48	2.95	3.30	2.53	2.71	2.53	2.78	3.45	2.74	2.76	2.75	2.31
Lu	0.45	0.34	0.45	0.52	0.40	0.42	0.40	0.44	0.54	0.42	0.43	0.43	0.37
Hf	4.84	3.80	5.08	4.92	4.90	5.72	3.99	4.82	6.54	8.28	7.49	4.78	3.96
Ta	0.86	0.90	0.94	0.76	0.83	0.95	0.61	0.75	1.16	1.58	1.45	0.75	0.72
Pb					9.03	6.51	5.05	19.70	9.65	9.07	23.38	1.45	4.45
Th	1.90	2.03	2.42	1.72	2.06	2.91	1.05	1.87	3.40	5.98	5.12	1.04	0.91
U	0.45	0.44	0.56	0.46	0.47	0.48	0.33	0.70	1.96	1.13	0.84	0.28	0.23
$(La/Yb)_N$	10.8	14.3	12.3	12.6	13.0	14.3	7.8	9.0	11.9	25.1	21.6	6.5	7.1

Table 2
Sr–Nd–Pb isotopic compositions of the Nandaling flood basalts

Sample	P1-8-2	P1-8-3	P1-8-4	P1-8-5	P1-11-1	P1-12-1	P1-12-2	P1-14-1	P1-14-3	P1-16-1	P1-16-2	P1-16-3	P1-16-4
Rb (ppm)	4.8	50.7	13.6	58.6	10.2	56.5	29.8	98.2	232.1	163.7	99.4	94	11.5
Sr (ppm)	757.47	447.23	1207.92	524.25	2052.01	770.58	827.25	294.64	68.95	197.22	1346.07	54.83	1987.89
$^{87}Rb/^{86}Sr$	0.018	0.328	0.032	0.323	0.014	0.212	0.104	0.964	9.756	2.402	0.214	4.962	0.017
$^{87}Sr/^{86}Sr$	0.708073	0.706580	0.705531	0.705820	0.704963	0.705451	0.705195	0.706939	0.724810	0.709524	0.705638	0.714215	0.704823
$\pm 2\sigma$	20	19	15	19	15	12	19	20	25	30	13	19	15
$(^{87}Sr/^{86}Sr)_i$	0.708024	0.705694	0.705445	0.704947	0.704925	0.704878	0.704914	0.704335	0.698453	0.703035	0.705060	0.700809	0.704777
Sm (ppm)	9.01	9.6	9.2	11.56	8.67	8.95	6.57	6.93	10.09	12.34	10.66	6.35	5.85
Nd (ppm)	41.62	49.38	43.36	63.33	47.89	49.03	32.17	36.73	55.57	77.61	64.5	30.79	28.05
$^{147}Sm/^{144}Nd$	0.1309	0.1175	0.1283	0.1104	0.1094	0.1103	0.1234	0.1141	0.1098	0.0961	0.0999	0.1247	0.1262
$^{143}Nd/^{144}Nd$	0.512224	0.512183	0.512110	0.511878	0.512057	0.511949	0.512206	0.512150	0.511951	0.511870	0.511813	0.512292	0.512277
$\pm 2\sigma$	13	13	13	15	15	13	14	14	15	14	14	15	11
$(^{143}Nd/^{144}Nd)_i$	0.512061	0.512037	0.511950	0.511741	0.511921	0.511812	0.512053	0.512008	0.511814	0.511751	0.511689	0.512137	0.512120
$\varepsilon_{Nd}(t)$	−6.5	−7.0	−8.6	−12.7	−9.2	−11.4	−6.7	−7.5	−11.3	−12.5	−13.8	−5.0	−5.3
Sample T_{DM} (Ga)	1.70	1.53	1.85	1.87	1.60	1.77	1.60	1.53	1.75	1.66	1.79	1.47	1.52
Source T_{DM}	1.86	1.78	2.02	1.99	1.69	1.88	1.74	1.63	1.86	1.73	1.88	1.59	1.61
$^{206}Pb/^{204}Pb$	16.872	16.884	16.813	16.127	16.651	16.492	16.542	16.114	16.275	16.442	16.389	16.852	16.529
$\pm 2\sigma$	18	30	9	10	11	11	8	22	13	19	70	10	33
$^{207}Pb/^{204}Pb$	15.327	15.325	15.292	15.203	15.275	15.248	15.256	15.202	15.176	15.208	15.237	15.263	15.251
$\pm 2\sigma$	19	34	9	13	12	11	8	27	14	20	70	12	34
$^{208}Pb/^{204}Pb$	36.882	36.915	36.750	36.086	36.601	36.511	36.425	36.057	36.029	36.422	36.369	36.719	36.403
$\pm 2\sigma$	20	34	10	13	12	12	9	30	14	20	70	15	34

mainly massive and amygdaloidal basalts with several interlayers of sandstone, tuffaceous sandstone and basaltic tuff. The samples were carefully collected and selected to avoid any involvement of sediment and tuff or minerals in the amygdaloid. The basalts display porphyritic and ophitic textures, and are composed dominantly of plagioclase and mafic minerals with minor amounts of quartz and iron oxides. Most of the mafic minerals were replaced by sericite, epidote and chlorite.

In the Nb/Y–Zr/TiO_2 diagram (Fig. 3), a widely-used plot involving elements considered to be more immobile, the NFB rocks mostly plot in the sub-alkaline basalt field, except for two samples plotting in the alkaline basalt field.

3. Analytical methods

Analyses for major, trace and rare-earth elements were performed at the Guangzhou Institute of Geochemistry,

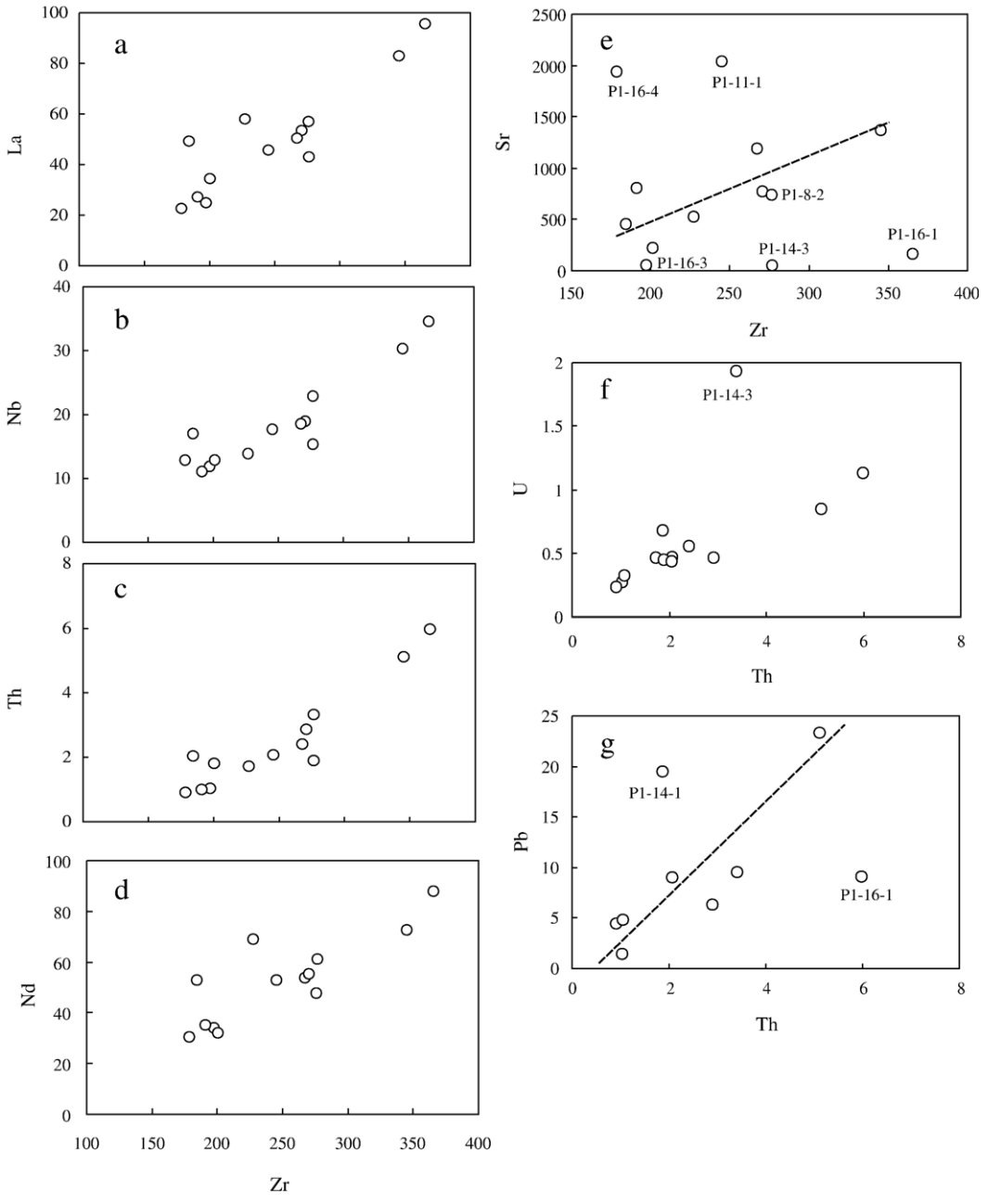


Fig. 4. Selected trace elements vs. Zr and Th diagrams for checking element mobility during post-eruptive alteration.

Chinese Academy of Sciences by ICP-AES and ICP-MS techniques. The detailed procedures have been documented in Li et al. (2002). Precision and accuracy are better than 1–10% for all major elements. Analytical precision for most trace elements is <3%, and reproducibility is generally <5%. Analyses of standards are

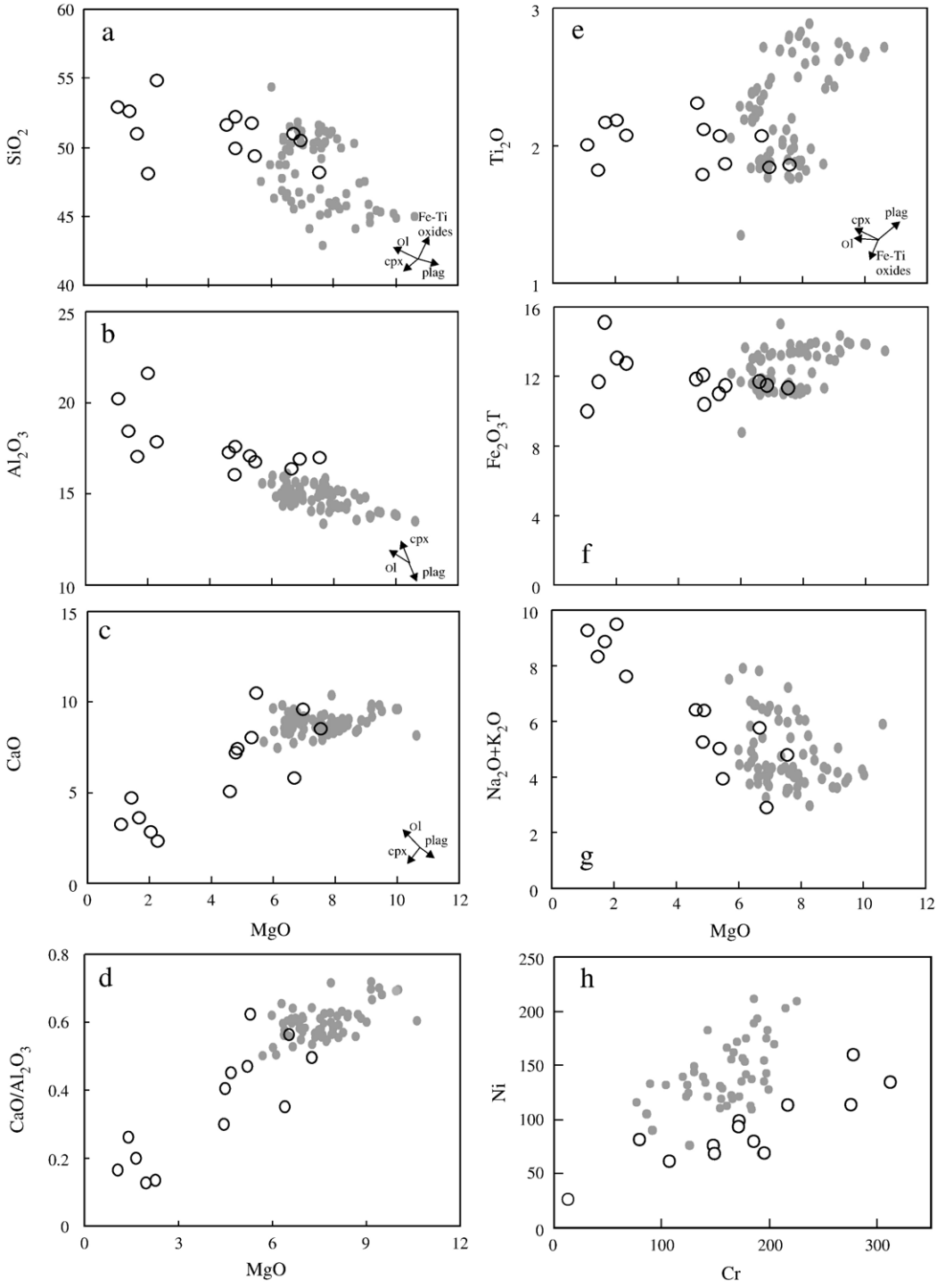


Fig. 5. Plots of MgO vs. other oxides, and Ni vs. Cr for the NFB, showing major-element variations with fractional crystallization (the trend is from Shaw et al., 2003). Oxide compositions of the NFB have been recalculated to 100% on anhydrous basis. The Hannuoba Cenozoic basalts (grey dots, Zhi et al., 1990; Basu et al., 1991) are shown for comparison.

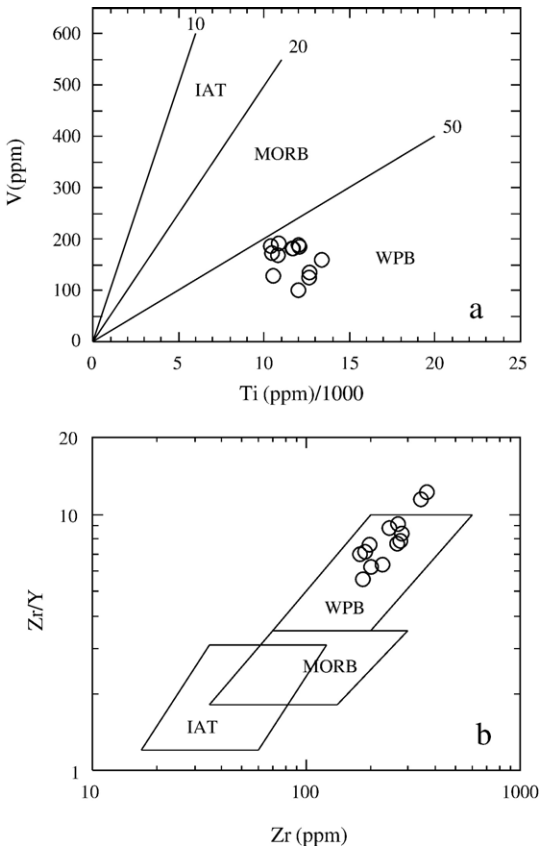


Fig. 6. V vs. Ti (a) and Zr/Y vs. Zr (b) diagrams for the NFB, illustrating their intraplate nature.

generally in good agreement with the recommended values.

Rb–Sr and Sm–Nd isotope analyses were performed on the VG-354 mass-spectrometer at the Institute of Geology and Geophysics, Chinese Academy of Sciences. The samples were dissolved in Teflon capsules using $HF+HClO_4$ acids. Rb, Sr, Sm and Nd were separated by cation-exchange technique. Procedural blanks for Rb–Sr and Sm–Nd isotope analyses were $2–5\times10^{-10}$ g and 5×10^{-11} g, and Sr and Nd isotopic compositions were normalized to $^{86}Sr/^{88}Sr=0.1194$ and $^{146}Nd/^{144}Nd=0.7219$, respectively. The measured $^{143}Nd/^{144}Nd$ values for the La Jolla and BCR-1 Nd standards were 0.511862 ± 7 (2σ, $n=12$) and 0.512651 ± 9 (2σ, $n=2$), respectively, and the measured $^{87}Sr/^{86}Sr$ value is 0.710254 ± 14 (2σ, $n=8$) for the NBS987 Sr standard. For Pb isotope determination, each sample (150 mg powder) was dissolved in the Teflon cup with HF acid. Pb was separated and purified by anion-exchange technique, and isotopic ratios were measured using the VG-354 mass-spectrometer at the Institute of Geology and Geophysics, Chinese Academy of Sciences. Procedural blank was <1 ng. Replicate analyses ($n=6$) for the NBS981 standard were $^{204}Pb/^{206}Pb$ $(1\sigma)=0.059003\pm0.000084$, $^{207}Pb/^{206}Pb$ $(1\sigma)=0.91439\pm0.00017$, and $^{208}Pb/^{206}Pb$ $(1\sigma)=2.16441\pm0.00097$. Major and trace element concentrations are listed in Table 1 and isotopic compositions are presented in Table 2.

4. Results

4.1. Hydrothermal alteration effects

The aforementioned petrography and the high loss on ignition (LOI) (2.46–6.79 wt.%, Table 1) in the NFB, suggest that the basalts had undergone hydrothermal alteration presumably during post-eruption processes. Thus, some elements may have been mobile. In a first approach, we investigate the mobility of Sr, Nd, Th, U and Pb. Since zirconium is an incompatible element for basaltic to andesitic lavas and Zr has generally been shown to remain stable during alteration or weathering

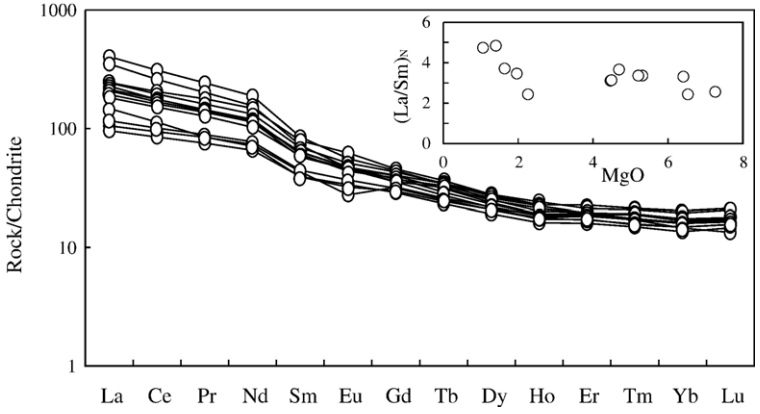


Fig. 7. Chondrite-normalized rare-earth-element patterns of the NFB. The insert is MgO vs. $(La/Sm)_N$ plot. Normalizing values are from Sun and McDonough (1989).

processes, it has been used as a reference to study the mobilities of other trace elements (Pearce et al., 1992).

In the La, Nb, Th and Nd vs. Zr variation diagrams (Fig. 4a–d), all the samples display coherent positive linear trends, suggesting relative immobilities of these elements during secondary alteration. Sr roughly correlates with Zr (Fig. 4e) for the samples with intermediate Sr (500–1400 ppm) contents, while the high Sr (1900–2000 ppm) and low Sr (50–200 ppm) samples plot away from the linear trend, owing to Sr mobility. The NFB plot in the U and Pb vs. Th diagrams (Fig. 4f–g) for investigating the relative mobility of Pb and U with respect to Th. The basalts display a positive linear trend in the U–Th plot except for the high U sample P1-14-3, suggesting that U was not heavily mobilized relative to Th. In the Pb vs. Th diagram, the basalts are roughly correlated except for two scattered samples. Element mobility can be further investigated on the primitive mantle-normalized patterns (Fig. 8a). In this diagram, the K and Sr elements display significant negative anomalies for some samples and positive anomalies for others, indicating their mobilities. Rb and Ba elements show systematic changes in spite of large variations compared with other elements, suggesting that they are not largely leached out or added in during alternation. As shown in the Pb vs. Th diagram, the Pb element is not highly mobilized since most of the samples have positive peaks.

In summary, alteration processes have not significantly affected high field strength elements (HFSE: Th, Nb, Zr, Hf, Ti, Y) or rare earth elements (REE). Their variations could be ascribed to magmatic processes and be used for geochemical characterization of the studied rocks. Sr and K elements were modified by alterations, and consequently, these two elements are excluded from the trace element dataset for the study of petrogenesis. Due to visible Sr mobility, Sr isotopes will be carefully screened.

4.2. Major elements

CIPW calculations show that the NFB are olivine- or quartz-normative, and have variable amounts of pyroxene- and feldspar-normative minerals. They show a

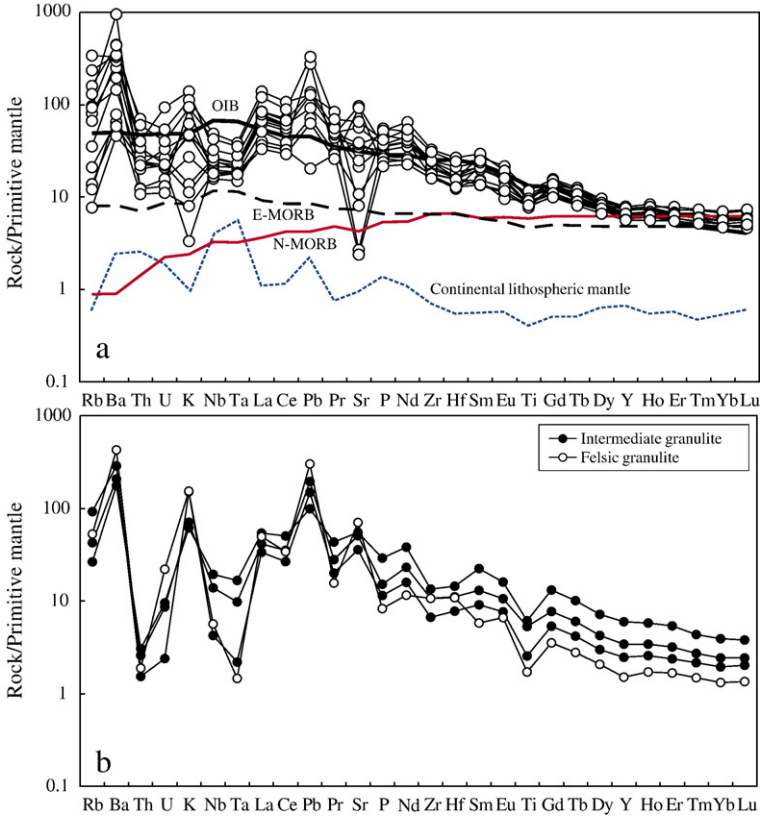


Fig. 8. Primitive mantle-normalized trace-element patterns for the NFB (a). The data for OIB, N-MORB, E-MORB and normalizing values are from Sun and McDonough (1989), continental lithospheric mantle (median composition of spinel peridotites) from McDonough (1990), and intermediate–felsic granulites (b) from Liu et al. (2001).

wide variation of SiO_2 (46.31–53.00 wt.%) and Mg# (20–60) (Table 1), and a limited variation of TiO_2 (1.73–2.24 wt.%) and Fe_2O_3 (mostly in the range of 10–12 wt.%) contents. The low MgO contents (7.27–1.06 wt.%) imply some fractional crystallization because none of the samples represents a primary magma with Mg# >68 in equilibrium with mantle olivine (Fo=88–92). Al_2O_3 (15.6–20.74 wt.%), P_2O_5 (0.45–1.15 wt.%) and $NaO+K_2O$ (2.75–9.17 wt.%) contents are high in the basalts. SiO_2 and Al_2O_3 display negative correlation with MgO whereas CaO exhibit positive correlation with MgO, suggesting the control of olivine and clinopyroxene fractionation (Fig. 5a–c). The positive correlation between $CaO/A1_2O_3$ and MgO (Fig. 5d) is characteristic of clinopyroxene fractionation. The total $NaO+K_2O$ contents decrease with increasing MgO (Fig. 5g). Plagioclase fractionation seems to be insignificant as revealed by major elements of the basalts. Fe–Ti oxides fractionation is also not pronounced (Fig. 5e–f). The Hannuoba Cenozoic lavas are generally plotted at the Mg-rich end along the trend defined by the Early Jurassic NFB, suggesting that these basalts are least-evolved primitive magmas and are not affected by the crustal processes during extrusion. The variations of major-element compositions of the Hannuoba lavas can be explained by eclogite fractionation, namely, by fractionation of clinopyroxene, garnet and minor amounts of Fe–Ti-oxides (Zhi et al., 1990).

4.3. Trace elements

Ni (60–160 ppm), Cr (100–300 ppm) and Co (30–40 ppm) contents of the basalts are much lower than the values commonly assumed for primary magmas, demonstrating that the samples do not represent primary mantle melts but rather residual liquids that have fractionated from a more magnesium-rich parental magma, a common feature for most of the continental flood basalts (CFB) that are dominated by relative evolved basalts (Modeland et al., 2003). A distinct positive correlation between Ni and Cr contents (Fig. 5h) suggests fractionation of olivine and chromium spinel.

In tectonic discrimination diagrams, such as V–Ti (Fig. 6a) and Zr–Zr/Y plots (Fig. 6b), all the samples plot in the field of within-plate-basalt, consistent with their inferred eruption in an extensional intraplate environment. Chondrite-normalized REE patterns of the NFB (Fig. 7) are characterized by variable but pronounced LREE enrichment relative to HREE ($(La/Yb)_N$=6.5–25.1, N means chondrite-normalized). The absence of significant Eu anomaly (Eu/Eu*=1–1.3, except 0.7 for P1-16-3) and the lack of correlation between the magnitude of the small Eu anomaly and the degree of fractionation (e.g., MgO) suggest insignificant

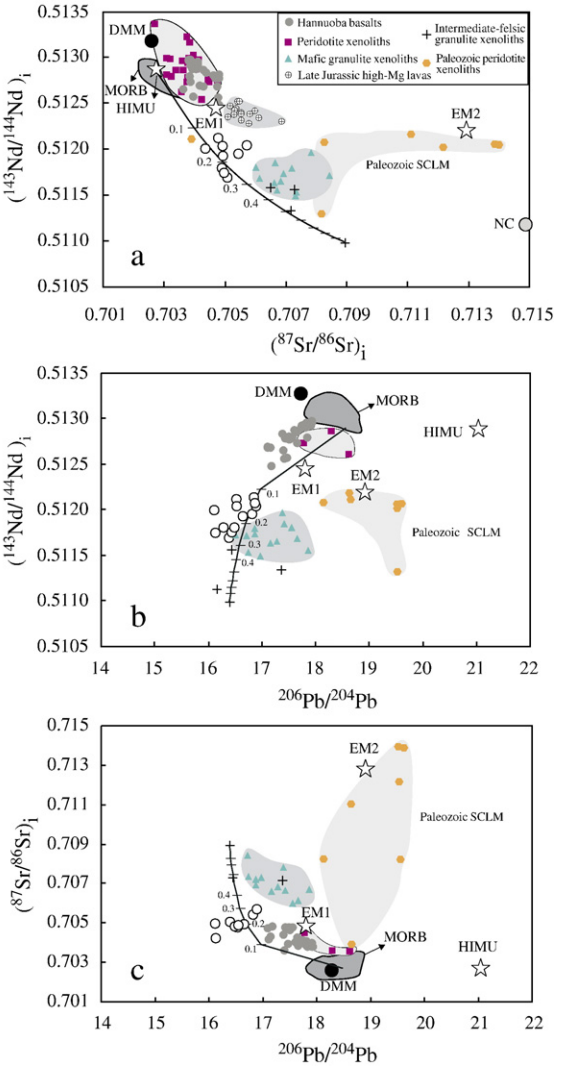


Fig. 9. $(^{87}Sr/^{86}Sr)_i$ vs. $(^{143}Nd/^{144}Nd)_i$ (a), $^{206}Pb/^{204}Pb$ vs. $(^{143}Nd/^{144}Nd)_i$ (b) and $(^{87}Sr/^{86}Sr)_i$ (c) diagrams for the NFB (t=190 Ma). The MORB field is from Hoffmann (1997). DMM, HIMU, EM1 and EM2 compositions are from Hollanda et al. (2006) and references therein. The data for the Hannuoba basalts are from Song et al. (1990), Basu et al. (1991); peridotite xenoliths from Song and Frey (1989), Tatsumoto et al. (1992), Liu et al. (1996), Rudnick et al. (2004); mafic granulite xenoliths from Zhou et al. (2002); intermediate–felsic granulite xenoliths from Liu et al. (2004a,b); Paleozoic kimberlite-borne mantle peridotite xenoliths from Zheng and Lu (1999); and Late Jurassic high-Mg lavas and the North China crust (NC) from Gao et al. (2004). The solid lines with hatch marks are mixing curves between upper mantle with the isotopic composition of MORB and an intermediate granulite (DMP-27), and the numbers next to the curves indicate the percentage of the lower crust in the mixing system. See detailed discussion in the text.

fractionation of plagioclase. The total REE concentrations and the slope of normalized patterns ($(La/Sm)_N$) increase with increasing differentiation (insert of Fig. 7). The systematic variation of LREE and relative constant HREE ($(Dy/Yb)_N = 1.4–1.5$) conform fractional crystallization during extrusion from a homogeneous source for the basalts.

The NFB have similar primitive mantle-normalized trace-element patterns. They are characterized by marked Nb, Ta, Th, U and Ti troughs, and Ba and Pb peaks, a general feature often observed in continental flood basalts (e.g., Cox and Hawkesworth, 1985). Most of the other trace-element compositions are comparable with those of OIB (Fig. 8a).

4.4. Sr–Nd–Pb isotopes

The $(^{87}Sr/^{86}Sr)_i$ values ($t = 190$ Ma, see Section 2.3) of the NFB range from 0.7080–0.6985, mostly in the range of 0.704335–0.705694 (Table 2). Sample P1-8-2 has the highest initial value (0.708024). Duplicate analyses of this sample yield identical results. The high initial $^{87}Sr/^{86}Sr$ value in P1-8-2 may result from crustal contamination (see detailed discussion later). Three of the samples (P1-14-3, P1-16-1 and P1-16-3) have extremely high measured $^{87}Sr/^{86}Sr$ values (0.709524–0.724810) and extremely low $(^{87}Sr/^{86}Sr)_i$ ratios (0.698453–0.703035, Table 2). Moreover, their $(^{87}Sr/^{86}Sr)_i$ values strongly depend on the assigned age owing to their extremely high Rb/Sr ratios (1–4) as an indicator of post-eruption alteration. Together with their very low Sr contents (50–200 ppm, Table 2, Fig. 4e), we attribute the $(^{87}Sr/^{86}Sr)_i$ ratios of these three samples to alterations rather than inheritance from magma sources. Therefore, the Sr isotopic data of these four samples are not included in the discussion thereafter.

The $(^{143}Nd/^{144}Nd)_i$ ratios range from 0.511689 to 0.512137, and $\varepsilon_{Nd}(t)$ values are negative (−5.0 to −13.7). The highly negative $\varepsilon_{Nd}(t)$ values indicate that the NFB could be derived from an enriched mantle source or have extensively interacted with lithospheric components. On the diagram of $(^{87}Sr/^{86}Sr)_i$–$(^{143}Nd/^{144}Nd)_i$ (Fig. 9a), the data of the NFB plot below the mantle array defined by mantle-derived rocks, and extend from EM1 to low $(^{143}Nd/^{144}Nd)_i$ trend.

The NFB display extremely low $(^{206}Pb/^{204}Pb)$ (16.1–16.9), $(^{207}Pb/^{204}Pb)$ (15.2–15.3) and $(^{208}Pb/^{204}Pb)$ (36.0–36.9). The limited ranges and coherent variations in the Pb isotopic ratios (Fig. 10a–b) suggest that the low or non-radiogenic Pb isotopic ratios are inherited from magma sources. Previous research indicated that it could be a distinctive nature of the Mesozoic mafic rocks in the NCC (e.g., Zhang et al., 2002).

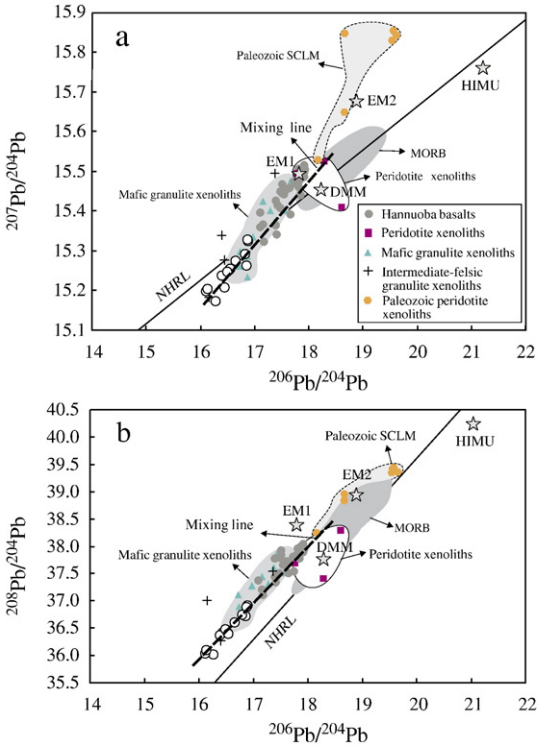


Fig. 10. Plots of $^{206}Pb/^{204}Pb$ vs. $^{207}Pb/^{204}Pb$ (a) and $^{206}Pb/^{204}Pb$ vs. $^{208}Pb/^{204}Pb$ (b) for the NFB. NHRL (north hemisphere reference line) is from Hart (1984). The sources for other data are the same as those in Fig. 9.

5. Discussion

The Nandaling basalts are characterized by pronounced Nb, Ta, Th, U and Ti depletions, LREE, Ba and Pb enrichments on primitive-mantle normalized patterns, moderate Sr, and low Nd and Pb initial isotopic ratios. Namely, they display a distinctive lithospheric signature (e.g., depleted in HFSE and enriched in LREE) compared with oceanic basalts (OIB and MORB). In general, there are several petrogenetic interpretations for this kind of lithospheric signature: (1) melting of enriched subcontinental lithospheric mantle (SCLM) (e.g., Hergt et al., 1991; Brewer et al., 1992; Lightfoot et al., 1993; Garland et al., 1996); (2) crustal contamination (e.g., Ellam and Cox, 1989); (3) interaction between asthenospheric magma and subcontinental lithospheric mantle (e.g., Ellam and Cox, 1991; Frey et al., 1996); and (4) combinations of some of these processes (e.g., Arndt and Christensen, 1992). In the following, we address the cause for the lithospheric signature in the NFB and their petrogenesis.

5.1. Assessment of crustal contamination

The NFB erupted in a continental setting, and an assimilation–fractional crystallization (AFC) (DePaolo, 1981) process was likely involved. The studied samples have much higher abundances of Sr (mostly 500–2000 ppm, excluding the lowest Sr samples that have obviously been affected by alteration as aforementioned), and Nd (30–90 ppm) than average compositions of crustal rocks (Sr 300–350 ppm, Nd 10–25 ppm, Rudnick and Fountain, 1995), suggesting that they may be immune to crustal assimilation (e.g., O'Brien et al., 1995). Nevertheless, it is still necessary to assess the effect of crustal contamination on the basalts.

A general way for testing whether the geochemistry of the rocks has been modified by crustal contamination during magma differentiation, is to plot trace element concentrations and isotopic ratios against an index of differentiation, such as MgO. On the diagrams of $(^{87}Sr/^{86}Sr)_i$–MgO and $(^{143}Nd/^{144}Nd)_i$–MgO (inserts in Fig. 11a–b), the basalts plot in complicated patterns, and it is not easy to distinguish the effect of AFC processes. Consequently, we appraise AFC by plotting the Sr–$(^{87}Sr/^{86}Sr)_i$ and Nd–$(^{143}Nd/^{144}Nd)_i$ diagrams (Fig. 11a–b). Sample P1-16-4 is selected as an end member for the mafic magmas, since it has the highest Mg# and $(^{143}Nd/^{144}Nd)_i$, and lowest $(^{87}Sr/^{86}Sr)_i$ (Tables 1 and 2), and could be regarded as the least contaminated and evolved sample for the NFB.

Before we choose a suitable end member for crustal contaminants, it is necessary to briefly evaluate the compositions of crustal rocks in the study area. Available crustal components in the Yanshan belt as potential contaminants are: lower crustal granulite xenoliths recovered from the Cenozoic Hannuoba basalts (e.g., Zhou et al., 2002; Liu et al., 2004a,b) near the study area (Fig. 1), exposed Archean granulites (Zhou et al., 2002; Liu et al., 2004a,b) and amphibolites (Jiang, 2005), and average isotopic composition of the North China crust (NC, Gao et al., 2004).

In the $(^{87}Sr/^{86}Sr)_i$–$(^{143}Nd/^{144}Nd)_i$ plot (Fig. 9a), the samples plot in the lower part of EM1 quadrant, far away from any mixing trend between mantle reservoirs and upper crust (EM2). Therefore, significant upper crustal contamination is not a possibility. The exposed Archean granulites, amphibolites and NC are also not suitable candidates due to their lower Sr (<500 ppm) and Nd (<30 ppm) contents than most of the basalts (Fig. 11a–b). Mafic granulite xenoliths have comparable Sr (400–1800 ppm), but lower Nd (<25 ppm) contents than those of the NFB. The formation age of these mafic granulites at 80–180 Ma as products of basaltic underplating (e.g., Wilde et al., 2003; Liu et al., 2004a,b), is later than the formation age of the NFB, which excludes them to be a contaminant for the NFB. Thus, an appropriate crustal end member seems to be the intermediate–felsic granulite xenoliths.

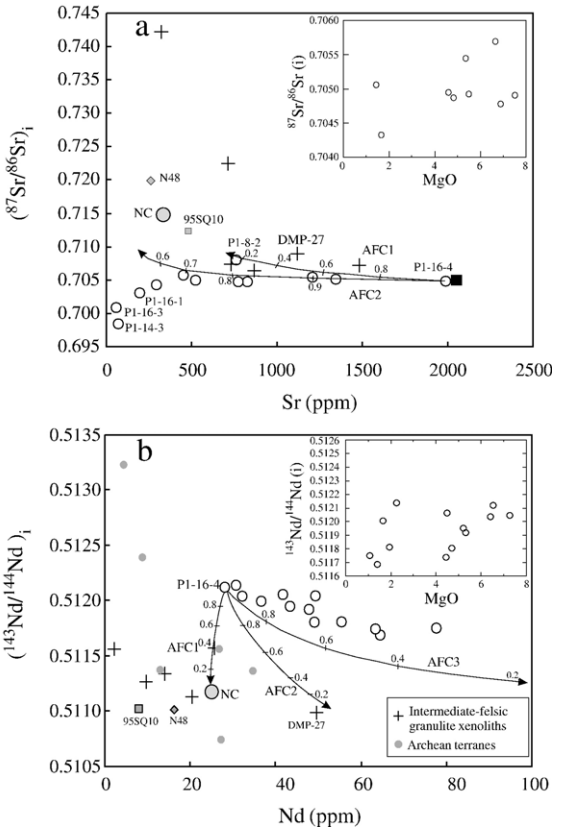


Fig. 11. Sr vs. $(^{87}Sr/^{86}Sr)_i$ (a) and Nd vs. $(^{143}Nd/^{144}Nd)_i$ (b) diagrams for assessing the effect of crustal contamination. The inserts are $(^{87}Sr/^{86}Sr)_i$–MgO and $(^{143}Nd/^{144}Nd)_i$–MgO plots for the NFB. Crustal components: lower crustal granulites (intermediate–felsic granulite xenoliths, Liu et al., 2004a,b), exposed Archean terrane granulites (Liu et al., 2004a,b; 95SQ10 — Zhou et al., 2002), exposed Archean amphibolite (N48, Jiang, 2005), average isotopic composition of the North China crust (NC, Gao et al., 2004). The hatch marks with numbers on the AFC curves indicate the percentage of melt left in the system ('*F*' value). See details in the text.

U–Pb zircon dating demonstrated that the protoliths of the intermediate–felsic granulites formed in the Precambrian (1.8–1.9 Ga for felsic, 2.5 Ga for intermediate granulites, Liu et al., 2004a,b). Two of the reported granulites have zircon $^{206}Pb/^{238}U$ ages of 192–193 Ma (Wilde et al., 2003; Liu et al., 2004a,b), identical to the eruption age of the NFB. On primitive mantle-normalized patterns, the intermediate–felsic granulites display pronounced Nb, Ta, Th, U and Ti

troughs, and Ba and Pb peaks, a similar geochemical signature to those of the NFB (Fig. 8). They have high Sr (300–1500 ppm) and $(^{87}Sr/^{86}Sr)_i$ ratios (0.7065–0.7422), and low $(^{143}Nd/^{144}Nd)_i$ (0.5110–0.5116) and Pb isotopic ratios (16.1–17.4) (Liu et al., 2004a,b, recalculated to 190 Ma for initial Sr and Nd isotopic values). All these characteristics suggest that the intermediate–felsic granulites could be an exclusive crustal component as a contaminant for the NFB. Therefore, we select one of the intermediate granulites (DMP-27) as the crustal end member.

Results of the AFC examination are given in Fig. 11a–b. The AFC1 curve in Fig. 11a, using high D_{Sr} (1.3) and r (0.5), is successful for the sample of P1-8-2, which has the highest $(^{87}Sr/^{86}Sr)_i$ value (0.708024). To explain other samples by the AFC2 curve (r=0.5), D_{Sr} needs to be 3.2, which is unrealistically too high for mafic lavas (Rollinson, 1995). The extremely low $(^{87}Sr/^{86}Sr)_i$ samples (P1-14-3, P1-16-1 and P1-16-3) with high measured $^{87}Sr/^{86}Sr$ values cannot be modeled by AFC process using any of the parameters, indicating their Sr isotopic compositions were modified by alteration as mentioned before. In Fig. 11b, the AFC curves fail to explain Nd-isotopic ratios and Nd content in the NFB. Both the AFC1 (D_{Nd}=1.01, r=0.5, specifically using the NC as the crustal end member) and AFC2 (D_{Nd}=0.95, r=0.5) curves are far away from the trend defined by the NFB. The AFC3 curve (D_{Nd}=0.55, r=0.5) roughly mimics the trend, but passes through none of the studied samples. In summary, an AFC process might be involved in the extrusion of the NFB, and partly affected Sr isotopes in some of the basalts. Nevertheless, it is unlikely that the AFC process plays a critical role in their petrogenesis.

5.2. Source region of the NFB

Melting of enriched SCLM is one of the possibilities for the lithospheric signature in the Early Jurassic NFB. The composition of the Pre-Mesozoic or Paleozoic lithospheric mantle beneath the NCC was commonly constrained using the Ordovician diamondiferous kimberlites and mantle peridotite xenoliths occurred in Mengyin of Shandong Province and Fuxian of Liaoning Province (e.g., Lu et al., 1997; Griffin et al., 1998; Zheng and Lu, 1999). Geochemical studies indicated that the kimberlite-borne mantle peridotites have high contents of incompatible elements and REE, implying an enriched SCLM in the Paleozoic (e.g., Lu et al., 1997). However, enriched SCLM seems unlikely to be a source for the NFB due to their extremely high LREE enrichment (Fig. 12a). Sr–Nd–Pb isotopes of the Paleozoic mantle peridotites are characterized by a distinctive trend to EM2 end member, clearly different from the trend defined by the NFB (Figs. 9 and 10). Hence, it is difficult to reconcile the geochemistry of the Early Jurassic NFB with the Paleozoic SCLM source. It is more likely that a new Mesozoic SCLM, in which the NFB might originate from, had partly replaced the Paleozoic one sometime after the Paleozoic (around 220 Ma, Gao et al., 2002).

The compositions of the Mesozoic SCLM could be identified by the mantle peridotite xenoliths recovered from the Hannuoba Cenozoic basalts (e.g., Gao et al., 2002; Rudnick et al., 2004). As seen from Fig. 12a, the trend constructed by the NFB is extrapolated into the field of these peridotite xenoliths, suggesting that the Mesozoic SCLM is probably a source for the NFB. On the other hand, the considerable overlap with the compositions of the NFB samples and the Hannuoba

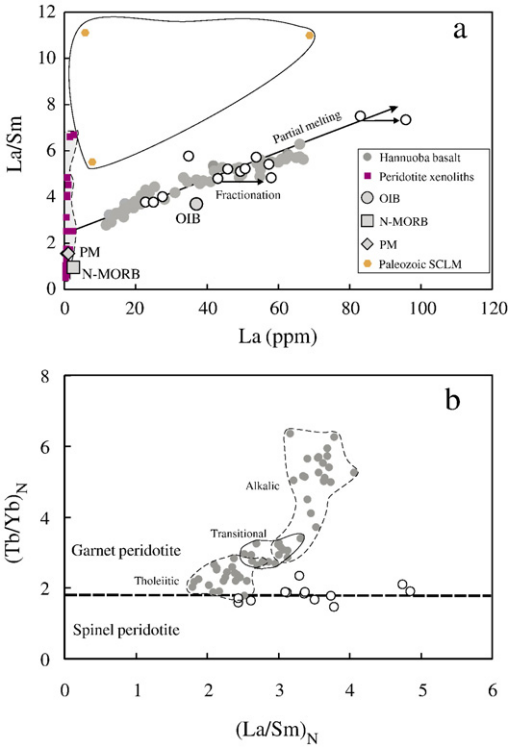


Fig. 12. La vs. La/Sm (a) and $(La/Sm)_N$ vs. $(Tb/Yb)_N$ (b) plots for the NFB. OIB, PM (primitive mantle) and N-MORB are from Sun and McDonough (1989); Hannuoba basalts from Zhi et al. (1990); peridotite xenoliths from Song and Frey (1989), Liu et al. (1996), Rudnick et al. (2004); Paleozoic kimberlite-borne mantle peridotite xenoliths from Lu et al. (1997). The horizontal dashed line in (b) separates fields expected for melting garnet- and spinel-bearing peridotite as determined for the Cenozoic basalts in the Basin and Range province (Wang et al., 2002).

basalts suggests that the Mesozoic SCLM may compositionally be comparable to that of the Cenozoic counterpart that generates the Hannuoba tholeiitic lavas via partial melting (Song et al., 1990).

In the $(La/Sm)_N$ vs. $(Tb/Yb)_N$ diagram (Fig. 12b), the NFB samples plot along the transitional zone from spinel to garnet peridotite, while most of the Hannuoba basalts plot in the field of garnet peridotite. This observation is consistent with the absence of HREE depletion in the NFB and the pronounced HREE depletion in the Hannuoba basalts, suggesting a spinel–garnet transitional peridotite mantle source for the NFB, and fractionation of garnet (Zhi et al., 1990) or the contribution of garnet in the deep mantle during partial melting for the Cenozoic basalts (Basu et al., 1991). The transition from spinel to garnet lherzolite occurs at 2.4–2.7 GPa in peridotite of MORB pyrolite composition (e.g., Green and Ringwood, 1967; Klemme and O'Neill, 2000), and at 2.8–3.1 GPa in depleted peridotite (Robinson and Wood, 1998), implying that the NFB magmas formed at least at 70–80 km depth. Even though these REE data suggest that the NFB are derived by partial melting over a depth range in the garnet–spinel transition zone of the Mesozoic SCLM, we still hesitate to attribute the lithospheric signature to their SCLM source since there is no agreement on this contentious subject at present. It is noting that the compositions of the SCLM are typically characterized by Nb (Ta) enrichment on the primitive mantle-normalized patterns (McDonough, 1990), which is strikingly distinct from the NFB samples (Fig. 8a).

5.3. Partial melting modeling

The degree of partial melting (f) and source compositions from primitive magmas can be obtained using the dynamic melting inversion (DMI) method (Zou and Zindler, 1996; Zou et al., 2000). This method uses variations of between-magma concentration ratios (Q) for two incompatible elements that have different bulk partition coefficients. The advantage for this approach is that the degrees of partial melting and source compositions can be calculated independently. For dynamic partial melting inversion, the highly incompatible element has bulk partition coefficient D_a about 0.001, and the ideal D_b for the less-so-highly incompatible element would be between 0.01 and 0.1 so that Q_b is different enough from Q_a and from 1.0. Thus, La is suitable for D_a, and Nd, Sm, Eu, Gd, and Tb are suitable for D_b.

The DMI method requires that selected lavas have high Mg# to avoid extensive fractional crystallization. Among the thirteen NFB samples, five have Mg# between 20 and 30, another five have Mg# ranging from 47 to 52, and only three samples have Mg # between 57 and 60 (Table 1). We thus choose the three samples (P1-12-2, P1-16-4 and P1-8-3) with high Mg# for inversion. These three samples also have similar Nd and Sr isotopic compositions. Another requirement for the DMI method is that the low-degree/high-degree concentrations ratios regularly decrease with the increase of their bulk partition coefficients. The pair of P1-12-2 and P1-16-4 satisfies these DMI requirements. The La concentration ratio (P1-12-2)/(P1-16-4) is taken as Q_a, and the Sm concentration ratio is used to derive Q_b for this pair:

$$Q_a = Q_{La} = 27.51/22.73 = 1.210$$

$$Q_b = Q_{Sm} = 6.798/6.013 = 1.131$$

Using these concentration ratios and melting porosity $\phi = 1\%$ (McKenzie, 1985), and solving the system of Eqs. (3), (4) and (5) in Zou et al. (2000), we have $f_1 = 4.67\%$ for P1-12-2 and $f_2 = 5.53\%$ for P1-16-4. Similarly, using the La concentration ratio for Q_a, but Nd, Eu, Gd, or Tb (instead of Sm) to obtain Q_b, four additional sets of f_1 and f_2 can be obtained. Averaging all the obtained values yields $f_1 = 4.33\%$ and $f_2 = 5.15\%$. The average degrees of melting are used to calculate source concentrations (C_0) for La, Nd, Sm, Eu, Gd, and Tb according to Eq. (1) in Zou et al. (2000) (Table 3). The DMI results clearly demonstrate a small degree (4 to 5%) partial melting of an LREE-enriched source.

The degrees of partial melting can also be obtained from other sample pairs. The pair of P1-8-3 and P1-12-2 yields average degree of melting 2.21% for P1-8-3 and 4.09% for P1-12-2 (Table 3). The pair of P1-8-3 and P1-16-4 gives the average degree of melting 2.31% for P1-8-3 and 5.01% for P1-16-4 (Table 3). It is noted that results of degrees of melting and source concentrations from the three pairs are consistent (Table 3). To sum up, the degrees of partial melting range from 2% to 5% for the three primitive lavas. Since P1-16-4 has the lowest La concentrations in all thirteen samples, its degree of partial melting (5%) is the maximum degree. The strong enrichments in LREEs relative to HREEs (Fig. 7) also argue for low degrees of partial melting, although in a qualitative sense. The melting degrees are low but the volumes of the mantle undergoing melting might be large. The magmas to form the Nandaling flood basalts might be extracted and accumulated from large volumes of mantle that undergo small degrees of melting.

Table 3
Calculation of partial melting degrees and source compositions for the Nandaling flood basalts

Elements	Bulk D	Low-f sample	High-f sample	Q (Low f/High f)	f_1 (%)	f_2 (%)	C_0	$(C)_0$
		P1-12-2	P1-16-4	(P1-12-2)/(P1-16-4)	$f_{P1\text{-}12\text{-}2}$	$f_{P1\text{-}16\text{-}4}$		
La	0.0021	27.51	22.73	1.210			1.00	4.23
Nd	0.0095	36.18	30.61	1.182	5.76	6.82	1.47	3.22
Sm	0.018	6.798	6.013	1.131	4.67	5.53	0.32	2.16
Eu	0.0228	2.132	1.949	1.094	3.26	3.92	0.11	1.96
Gd	0.0279	6.425	5.906	1.088	3.71	4.43	0.36	1.82
Tb	0.033	0.942	0.868	1.085	4.23	5.03	0.06	1.61
Ave. f					4.33	5.15		
		P1-8-3	P1-12-2	(P1-8-3)/(P1-12-2)	$f_{P1\text{-}8\text{-}3}$	$f_{P1\text{-}12\text{-}2}$		
La	0.0021	49.34	27.51	1.794			0.94	3.98
Nd	0.0095	52.86	36.18	1.461	1.44	3.00	1.40	3.07
Sm	0.018	9.647	6.798	1.419	3.31	5.68	0.31	2.08
Eu	0.0228	2.723	2.132	1.277	1.88	3.59	0.11	1.90
Ave. f					2.21	4.09		
		P1-8-3	P1-16-4	(P1-8-3)/(P1-16-4)	$f_{P1\text{-}8\text{-}3}$	$f_{P1\text{-}16\text{-}4}$		
La	0.0021	49.34	22.73	2.171			0.97	4.11
Nd	0.0095	52.86	30.61	1.727	2.02	4.51	1.41	3.09
Sm	0.018	9.647	6.013	1.604	3.10	6.35	0.31	2.11
Eu	0.0228	2.723	1.949	1.397	1.80	4.17	0.11	1.95
Ave. f					2.31	5.01		

For the P1-8-3 and P1-12-2 pair and P1-8-3 and P1-16-4 pair, Gd and Tb have higher Q than Eu, thus the results for Gd and Tb are not used for the calculation of average f.

Because Sm/Nd ratios in melts are smaller than source Sm/Nd ratios, sample Nd model ages are minimum ages. Source Sm and Nd concentrations calculated from DMI can be used to better constrain the source Nd model ages (Zou et al., 2003). According to DMI results, source Sm/Nd=0.32/1.47=0.1311, which is about 12%, 6.6%, and 4.4% higher than sample Sm/Nd ratios in P-12-2, P1-8-3, and P1-16-4. Source Sm/Nd ratios for other fractionated samples cannot be calculated directly from the DMI method. However, if we assume that source Sm/Nd ratios are in average 6% higher than their sample Sm/Nd ratios based on the above DMI calculations, source Nd model ages can be estimated and are presented in Table 2. The source Nd model ages range from 1.6 to 2.0 Ga, about 10% higher than sample Nd model ages (1.5–1.9 Ga).

5.4. Identification of the lower crustal component and crust–mantle interaction

As aforementioned, the NFB samples plot in the lower part of EM1 quadrant in the $(^{87}Sr/^{86}Sr)_i$–$(^{143}Nd/^{144}Nd)_i$ diagram (Fig. 9a), and have primitive mantle-normalized patterns similar to those of the Precambrian intermediate–felsic granulites (e.g., pronounced Nb, Ta, Th, U and Ti troughs, and Ba and Pb peaks) (Fig. 8), suggesting that the lithospheric imprint in the NFB may be attributed to the involvement of lower crustal materials, which typically have low Sr and Nd isotopic ratios and low Nb content (e.g., Stewart and Rogers, 1996; Morris et al., 2000). The addition of the intermediate–felsic granulites into the primitive magmas of the NFB systematically lowers the Nb and Th contents, as shown in Fig. 13. Ce/Pb and Nb/U ratios are useful indicators to identify crustal component within continental basalts, since MORB and OIB have high and uniform values (25±5 and 47±10, Hofmann et al., 1986), whereas the continental crust displays much lower ratios (4 and 10, Hofmann et al., 1986). The Ce/Pb and Nb/U ratios in most of the NFB are lower than those in MORB and OIB (Fig. 14a). Together with the $(La/Sm)_{PM}$ vs. Nb/Th plot (Fig. 14b), the NFB samples give rise to a hyperbolic mixing trend between MORB-like magma and lower crustal granulites.

The extremely low Pb isotopic ratios in the NFB provide another clue for the involvement of the lower crust, since the lower crust is regarded as a major reservoir of unradiogenic Pb. Such unradiogenic Pb may be attributed to U depletion during granulite-facies metamorphism in the lower crust (e.g., Rudnick and Prespcr, 1990; Cohen et al., 1991). Correspondingly, the NFB samples define a straight mixing line between

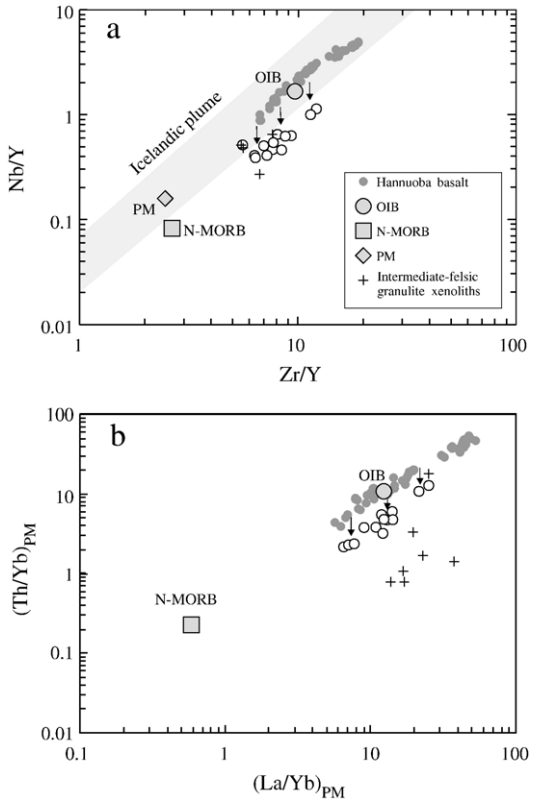


Fig. 13. Zr/Y vs. Nb/Y (a) and $(La/Yb)_{PM}$ vs. $(Th/Yb)_{PM}$ (b) diagrams. OIB, PM and N-MORB are from Sun and McDonough (1989); the field for Icelandic plume from Fitton et al. (1997); Hannuoba basalts from Zhi et al. (1990); and intermediate–felsic granulite xenoliths from Liu et al. (2001). The arrows show systematic shifts to lower Nb and Th contents due to addition of the lower crustal granulites.

MORB-like magma and lower crustal granulites in Pb isotopic plots (Fig. 10).

We present a simple model for the crust–mantle interaction using two end-members: upper mantle with an isotopic composition of MORB ($^{87}Sr/^{86}Sr/Sr$ [ppm]–$^{143}Nd/^{144}Nd/Nd$[ppm]–$^{206}Pb/^{204}Pb/Pb$[ppm]= 0.702725/502–0.512866/10.7–18.5/0.3, data sources from Gao et al., 2004 and references therein; Sun and McDonough, 1989; Hoffmann, 1997), and an intermediate granulite (DMP-27, $^{87}Sr/^{86}Sr/Sr$[ppm]–$^{143}Nd/^{144}Nd/Nd$[ppm]–$^{206}Pb/^{204}Pb/Pb$[ppm]=0.708932/1122–0.510985/49.5–16.395/7.01, Liu et al., 2001, 2004a,b). The modeling suggests that mixing of upper mantle with 15–25% (an average of 20%) lower crust could explain the Sr–Nd–Pb isotopic characteristics of the NFB (Fig. 9). Thus, the source Nd model ages (1.6 to 2.0 Ga) or sample Nd model ages (1.5–1.9 Ga) might result from the addition of the Precambrian intermediate–felsic granulites as dated by U–Pb zircons in the granulites (Liu et al., 2004a,b). Furthermore, the mixing modeling indicates that the feature AFC (Fig. 11) may also originate from this interaction.

5.5. Magmatic underplating and its role on the Mesozoic mafic rocks

Besides the AFC processes, there are two possibilities for the involvement of lower crust component in mantle-derived mafic rocks: (1) delamination and detachment of lower crust into underlying mantle and then recycling, and (2) magmatic underplating under the lower crust. Metamorphic reactions occurring in the lower continental crust (basalt→amphibolite→garnet clinopyroxenite/eclogite) can lead to density increase (up to 3.8 g/cm^3) and gravity instability of the overthickened lithospheric keel. It may detach from the uppermost lithosphere and founder into the upper mantle, and subsequently melt and interact with mantle peridotite. Partial melts of the metasomatized mantle would bear strong lower crust signatures and give rise to EMI-like basaltic magmatism (Lustrino, 2005). Such mechanism has been used to interpret the origin of the

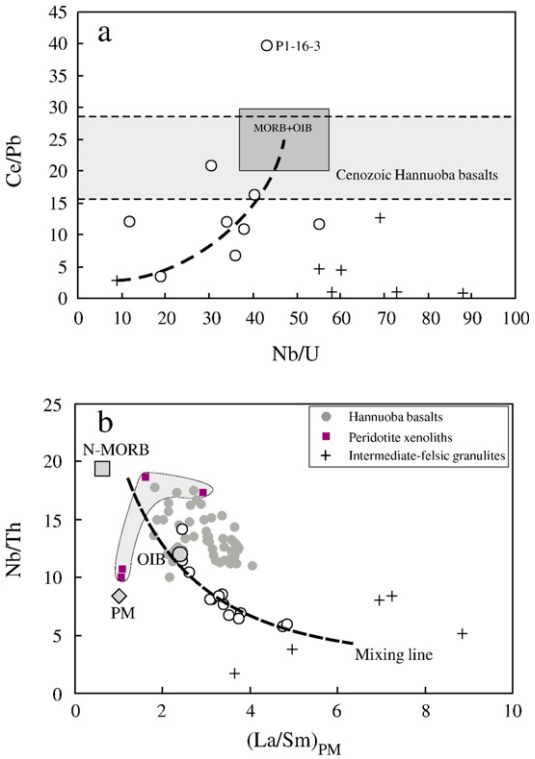


Fig. 14. Nb/U vs. Ce/Pb (a) and $(La/Sm)_{PM}$ vs. Nb/Th (b) plots showing mixing trends between MORB-like magma and lower crustal component.

Late Jurassic high-Mg andesites, dacites and adakites from the NCC (Fig. 9a, Gao et al., 2004). However, we do not favor a similar petrogenetic interpretation for the Early Jurassic NFB, due to the following considerations: (1) the foundered and recycled lower crust component is typically mafic in composition (e.g., Gao et al., 2004; Lustrino, 2005) rather than the intermediate–felsic counterpart as documented in this study, (2) partial melts of the metasomatized mantle after subsequent interaction between sunken lower crust and mantle peridotite would have high-Mg and high ε_{Nd} as seen in the Late Jurassic lavas, whereas the early Jurassic NFB samples are characterized by low-Mg and low ε_{Nd} (Tables 1 and 2, Fig. 9).

Underplating of mantle-derived magma and its interaction with the pre-existing continental lower crust is an important mechanism for lower crust evolution (e.g. Rudnick et al., 1986). Extensive studies of the basalt-borne lower crustal xenoliths have documented that basaltic underplating and subsequent crust–mantle interaction are preferable interpretation for formation of the lower crust in this region (e.g., Fan et al., 1998; Chen et al., 2001; Liu et al., 2001; Zhou et al., 2002; Liu et al., 2004a,b). U–Pb dating of zircons from these xenoliths provides a peak range at 80–180 Ma (Fig. 15b) (Wilde et al., 2003; Liu et al., 2004a,b), presumably recording the time of basaltic underplating (e.g., Liu et al., 2004a,b). However, the effect of the underplating and interaction on the mantle-derived magmas still remains to be clarified in the NCC. The striking similarity in age distributions of the Jurassic–Cretaceous mafic rocks to those of lower crustal xenoliths (Fig. 15) indicates a critical role of basaltic underplating and subsequent crust–mantle interaction on the evolution of these Mesozoic (especially pre-120 Ma) mafic rocks. Consequently, almost all the 120–190 Ma mantle-derived rocks bear strong EMI-like lower crust signatures (e.g., low Sr–Nd–Pb isotopic ratios) (Chen et al., 1997; Zhang et al., 2002, 2003, 2004; and this study).

5.6. A petrogenetic model for the NFB and its implications for lithospheric thinning

To initiate SCLM melting and generate various types of magmas (e.g., flood basalts), some external forces are generally required to be involved, including asthenosphere upwelling, lithospheric extension, thinning and decompression (McDonough, 1990). The northern margin of the NCC was tectonically dominated by extension during the Triassic and Early Jurassic as we documented in Section 2.2. The Mesozoic SCLM was thinned in response to extension, and the asthenosphere rose passively. It would trigger decompressional melting by the heat from the asthenosphere upwelling (e.g., Ruppel, 1995 and references therein). As for the NFB, the melting took place in the transitional zone from spinel to garnet peridotite at about 70–80 km depth. The melting products, namely basaltic magmas, would rise

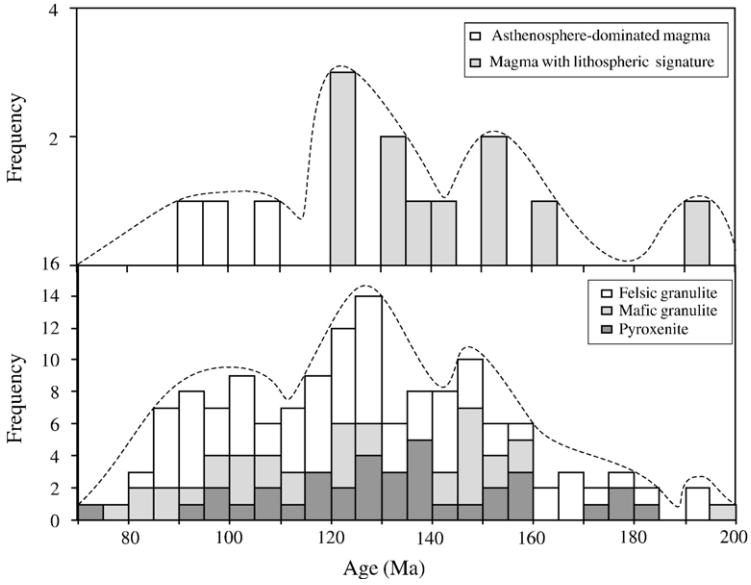


Fig. 15. Histogram of age distributions for the Jurassic–Cretaceous mantle-derived mafic rocks and lower crustal xenoliths in the Cenozoic Hannuoba basalts. Data sources for mafic rocks are from Chen et al. (1997), Zhao et al. (2002), Zhang et al. (2003, 2004 and references therein); for lower crustal xenoliths from Wilde et al. (2003), Liu et al. (2004a,b).

into and stagnate at the crust–mantle boundary owing to the low density of the continental crust. As a result, extensive interaction between the underplating basaltic magmas and the lower crust largely modified the compositions of the primitive magmas, and gave rise to a distinctive EM1-like lithospheric signature. Some of the interacted magmas eventually erupted as flood basalts (Fig. 16).

The mechanism and geodynamics associated with the Mesozoic lithospheric thinning or replacement beneath the NCC are still hotly debated. Whole-scale delamination is not a favored mechanism, on the basis of density contrast and detailed seismic tomography (e.g., Yuan, 1996; Xu, 2001). The correlation of lithospheric thinning with breakup and dispersal of Gondwanaland was mainly based on a comparable time sequence recorded in both regions (Wilde et al., 2003). Mesozoic volcanism during the break-up and dispersal of Gondwana, for example, the 185–60 Ma continental flood basalts, is mostly mantle plume-related (Hawkesworth et al., 1999). It is, however, not the case in the NCC (e.g., Xu, 2001).

Xu (2001) proposed that the onset of lithosphere destruction was coincident with the Triassic collision between the North China and Yangtze blocks along the Qiling–Dabie orogenic belt. He considered the collision as a trigger to destroy the physical integrity of the NCC, and the coupled thermo-mechanical and chemical erosion (Menzies and Xu, 1998) as an important mechanism to replace the old lithospheric keel by "oceanic" mantle, in a way of gradual upward migration or along mushroom cloud-like lithosphere–asthenosphere boundary (Yuan, 1996; Lu et al., 2000). Zheng et al. (2001) also put forward that lithospheric thinning was accompanied by the aforementioned collision at 220 Ma, but resulted from mechanical rifting in an extensional regime, allowing upwelling of asthenospheric materials, and leading to a dispersal and dilution of the old subcontinental lithospheric mantle (Yuan, 1996; O'Reilly et al., 2001). Obviously, the Triassic collision between the North China and Yangtze blocks was highlighted in both of the models. However, the occurrence of intraplate mantle-derived volcanism in the northern margin (Early Jurassic) of the NCC was earlier than that in the southern margin (~120 Ma, e.g., Zhang et al., 2003), where the Triassic collision executed. Therefore, the proposal of the Triassic collision between the North China and Yangtze blocks as a trigger for lithospheric thinning is inconsistent with the reverse diachronous occurrence of the mantle-derived volcanism. The thinning time in the northern margin (Early Jurassic) seems to be earlier than that in the southern margin (Early Cretaceous), if the mantle-derived volcanism is an indicator of lithospheric modification.

Zhang et al. (2003) presented a complicated geodynamic model for interpreting replacement processes. They suggested that: (1) Paleozoic oceanic subduction beneath both the northern and southern margins of the NCC destabilized the eastern NCC, and initiated thinning and replacement of the lithospheric mantle; (2) the thinning process continued during Mesozoic continental subduction and continent–continent collision, and climaxed in the Cretaceous; (3) interaction between the refractory lithospheric mantle and slab-derived silicic melts formed a Mesozoic fertile lithospheric mantle where the Mesozoic mafic volcanic rocks were derived; and (4) the Mesozoic mantle was again replaced by an oceanic lithospheric mantle during the Cenozoic by delamination of the subcontinental lithospheric mantle and accretion of upwelling

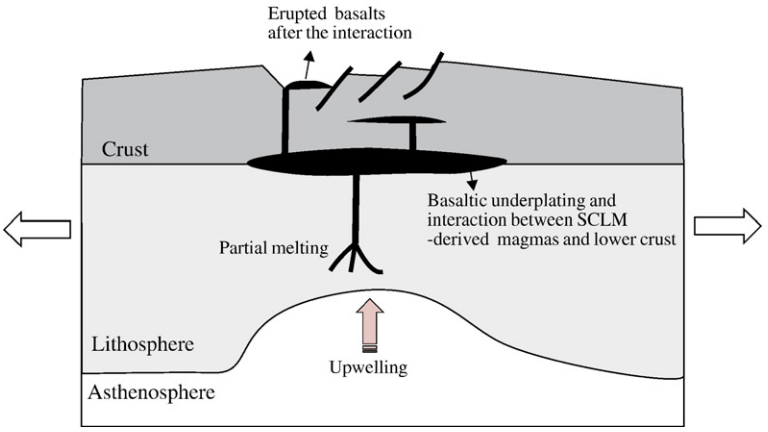


Fig. 16. A schematic petrogenetic model for the NFB, incorporating the processes of asthenosphere upwelling, partial melting of the SCLM, basaltic underplating and interaction between mantle-derived magmas and lower crust, and lithospheric extension.

asthenospheric materials. Detailed evaluation of this model is beyond the scope of this paper. Their suggestion was mainly based on an observation that the lithospheric mantle beneath the center of the craton was less modified than that of the margins. It is unconvincing to correlate the lithospheric thinning with circum-NCC subduction processes. Actually, the overall NCC is in an intraplate setting from 220 Ma on, including the main stage of the thinning (180–80 Ma, Wilde et al., 2003), and the subduction zones in process were near 1000 km away from the NCC (Fig. 1).

Analysis of tectonic sequences on the southern margin of the NCC indicated that post-orogenic extension occurred in the Early Cretaceous, and was contemporary with the development of intraplate mantle-derived volcanism in this margin (e.g., Zhai et al., 2004), suggesting a similar tectonic–magmatic correlation with that in the northern margin. Therefore, lithospheric replacement or thinning in both margins may be a response to respective post-orogenic extension. In the passive model of continental rifting (e.g., Cortia et al., 2003 and references therein), the asthenosphere will passively rise as a consequence of extension. Then it triggers decompressional melting of the mantle by the heat from the asthenosphere upwelling, and generates mantle-derived volcanism and magmatic underplating at the crust–mantle boundary.

Geochemical investigation of the Mesozoic mantle-derived rocks in the NCC demonstrated that the lithospheric signature is dominant prior to about 110 Ma, but diminished (asthenosphere-dominated) after that time (Zhang et al., 2003; Fig. 15a). This temporal decrease in a lithospheric signature, also a typical feature of some continental flood basalts (e.g., Hawkesworth and Gallagher, 1993), implies consumption of lithospheric mantle by partial melting and upwelling of the asthenosphere. Consequently, the lithosphere beneath the NCC was extensively thinned, coupled with the loss and replacement of lower crust by magmatic underplating and crust–mantle interaction. This kind of correlation between lithospheric thinning and magmatic underplating could also be a major process in some of famous continental rifts, such as the East African Rift (Karson and Curtis, 1989; Hendrie et al., 1994; Mechie et al., 1994) and the Basin and Range Province (e.g., Gans, 1987; Hauser et al., 1987; Parsons, 1995; MacCready et al., 1997).

It is noted that the northern margin of the NCC, including the Yanshan belt, was tectonically dominated by contractional deformation during the Late Jurassic–Early Cretaceous (about 160–120 Ma; e.g., Zheng et al., 2000; Davis et al., 2001a). However, magmatic underplating, replacement of lower crust and lithospheric thinning continued during the stage of crustal shortening, as demonstrated by age spectrums for lower crustal xenoliths and mantle-derived magmatism (Fig. 15). This decoupling between surface tectonics and lithospheric evolution implies that: (1) asthenosphere upwelling and magmatic underplating played a dominant role in the main process of lithospheric replacement or thinning; and (2) the contractional deformation is of thin-skinned tectonic style (e.g., Davis et al., 2001a), and lower or middle crustal flow in the Yanshan belt is expected to be similar to that in the Basin and Range Province (e.g., MacCready et al., 1997).

6. Conclusions

The present geochemical and Sr–Nd–Pb isotopic studies of the Early Jurassic Nandaling flood basalts in the Yanshan belt of the NCC lead to the following conclusions.

Geochemical characteristics of the NFB suggest that these sub-alkaline intraplate basalts are residual liquids that had fractionated from a more magnesium-rich parental magma through fractional crystallization of olivine and clinopyroxene during extrusion.

The primitive magma of the NFB originated from 2–5% partial melting of the transitional zone from spinel to garnet peridotite at depths of about 70–80 km in the Mesozoic SCLM.

The Nandaling flood basalts contain a distinctive lithospheric component and result from an interaction between lower crust (15–25%) and primitive magmas induced by magmatic underplating at crust–mantle boundary, rather than from crustal contamination, SCLM source or foundered and recycled lower crust.

Compiled geological analyses demonstrate that the NFB extruded in an extensional intraplate setting related to post-orogenic collapse in the northern margin of the NCC. The timing of lithospheric thinning in the northern margin (Early Jurassic) is earlier than that in the southern margin (Early Cretaceous) of the NCC, although both were triggered by respective post-orogenic extension.

The temporal similarity of the Jurassic–Cretaceous mantle-derived mafic rocks with EM1 imprint to lower crust replacement, and the decoupling of surface shortening with lithospheric modification during the Late Jurassic–Early Cretaceous, indicate a critical role of magmatic underplating and subsequent crust–mantle interaction accompanied by asthenosphere upwelling on the evolution of Mesozoic lithosphere of the NCC. The correlation between lithospheric thinning and magmatic underplating may be an important process in continental rifts.

Acknowledgements

This research was supported by the National Science Foundation of China (40132020 and 40572130). We are grateful for constructive comments by two anonymous reviewers and Editor Stephen Foley on an early version of this manuscript.

References

Arndt, N.T., Christensen, U., 1992. The role of lithospheric mantle in continental flood volcanism: thermal and geochemical constraints. J. Geophys. Res. 97, 10967–10981.

Badarch, G., Cunningham, W.D., Windley, B.F., 2002. A new terrane subdivision for Mongolia: Implications for the Phanerozoic crustal growth of Central Asia. J. Asian Earth Sci. 21, 87–110.

Basu, A.R., Wang, J., Huang, W., Xie, G., Tatsumoto, M., 1991. Major element, REE, and Pb, Nd and Sr isotopic geochemistry of Cenozoic volcanic rocks of eastern China: implications for their origin from suboceanic-type mantle reservoirs. Earth Planet. Sci. Lett. 105, 149–169.

Brewer, T.S., Hergt, J.M., Hawkesworth, C.J., Rex, D., Storey, B.C., 1992. Coats Land dolerites and the generation of Antarctic continental flood basalts. In: Storey, B.C., Alabaster, T., Pankhurst, R.J. (Eds.), Magmatism and the Causes of Continental Breakup. Geol. Soc. Lond. Spec. Publ., vol. 68, pp. 185–208.

Chen, Y.X., Chen, W.J., Zhou, X.H., Li, Z.J., Liang, H.D., Li, Q., Xu, K., Fan, Q.C., Zhang, G.H., Wang, F., Wang, Y., Zhou, S.Q., Chen, S.H., Hu, B., Wang, Q.J., 1997. Liaoxi and Adjacent Mesozoic Volcanics—Chronology, Geochemistry and Tectonic Settings. The Seismological Press, Beijing. (in Chinese with English abstract).

Chen, S., O'Reilly, S.-Y., Zhou, X.H., Griffin, W.-L., Zhang, G., Sun, M., Feng, J., Zhang, M., 2001. Thermal and petrological structure of the lithosphere beneath Hannuoba, Sino-Korean Craton, China: evidence from xenolith. Lithos 56, 267–301.

Cohen, A.S., O'Nions, R.K., O'Hara, M.J., 1991. Chronology and mechanism of depletion in Lewisian granulites. Contrib. Mineral. Petrol. 106, 142–153.

Cortia, G., Bonini, M., Conticelli, S., Innocenti, F., Manetti, P., Sokoutis, D., 2003. Analogue modelling of continental extension: a review focused on the relations between the patterns of deformation and the presence of magma. Earth-Sci. Rev. 63, 169–247.

Cox, K.G., Hawkesworth, C.J., 1985. Geochemical stratigraphy of the Deccan Traps at Mahabaleshwar, Western Ghats, India, with implications for open system magmatic processes. J. Petrol. 26, 355–377.

Darby, B.J., Davis, G.A., Zheng, Y., 2001. Structural evolution of the southern Daqing Shan, Yinshan belt, Inner Mongolia, China. In: Hendrix, M.S., Davis, G.A. (Eds.), Paleozoic and Mesozoic Tectonic Evolution of Central Asia: from Continental Assembly to Intracontinental Deformation. Geol. Soc. Am. Mem., vol. 194, pp. 199–214.

Davis, G.A., Wang, C., Zheng, Y., Zhang, J., Zhang, C., Gehrels, G., 1998. The enigmatic Yinshan fold-and-thrust belt of northern China: new views on its intraplate continental styles. Geology 26, 43–46.

Davis, G.A., Zheng, Y., Wang, C., Darby, B.J., Zhang, C., Gehrels, G., 2001a. Mesozoic tectonic evolution of the Yanshan fold and thrust belt, with emphasis on Hebei and Liaoning provinces, Northern China. In: Hendrix, M.S., Davis, G.A. (Eds.), Paleozoic and Mesozoic Tectonic Evolution of Central Asia: from Continental Assembly to Intracontinental Deformation. Geol. Soc. Am. Mem., vol. 194, pp. 71–197.

Davis, G.A., Zheng, Y., Zhang, C., Xu, B., 2001b. The Mesozoic Fengning–Longhua and Jiaoqier fault zone, North China: new interpretations of controversial structures. 2001 GSA Abstracts with Programs, A-49.

Deng, J.F., Zhao, G.C., Zhao, H.L., Luo, Z.H., Dai, S.Q., Li, K.M., 2000. Yanshanian igneous petrotectonic assemblage and orogenic-deep process in east China. Geol. Rev. 46, 41–48 (in Chinese with English abstract).

DePaolo, D.J., 1981. Trace element and isotopic effects of combined wallrock assimilation and fractional crystallization. Earth Planet. Sci. Lett. 53, 189–202.

Ellam, R.M., Cox, K.G., 1989. A Proterozoic lithospheric source for Karoo magmatism; evidence from the Nuanetsi picrites. Earth Planet. Sci. Lett. 92, 207–218.

Ellam, R.M., Cox, K.G., 1991. An interpretation of Karoo picrite basalts in terms of interaction between asthenospheric magmas and the mantle lithosphere. Earth Planet. Sci. Lett. 105, 330–342.

Fan, Q., Liu, R., Li, N., Sui, J., Lin, Z., 1998. Zircon chronology and REE geochemistry of granulite xenoliths at Hannuoba. Chin. Sci. Bull. 43, 1510–1515.

Fan, W.M., Zhang, H.F., Baker, J., Jarvis, K.E., Mason, P.R., Menzies, M.A., 2000. On and off the North China Craton: where is the Archaean keel? J. Petrol. 41, 933–950.

Fitton, G.J., Saunders, A.D., Norry, M.J., Hardarson, B.S., Taylor, R.N., 1997. Thermal and chemical structure of the Iceland plume. Earth Planet. Sci. Lett. 153, 197–208.

Frey, F.A., McNaughton, N.J., Nelson, D.R., deLaeter, J.R., Duncan, R.A., 1996. Petrogenesis of the Bunbury basalt, western Australia: interaction between the Kerguelen plume and Gondwana lithosphere? Earth Planet. Sci. Lett. 144, 163–183.

Gans, P.B., 1987. An open-system, two-layer crustal stretching model for the eastern Great Basin. Tectonics 6, 1–12.

Gao, S., Rudnick, R., Carlson, R.W., McDonough, W.F., Liu, Y.S., 2002. Re–Os evidence for replacement of ancient mantle lithosphere beneath the North China craton. Earth Planet Sci. Lett. 198, 307–322.

Gao, S., Rudnick, R.L., Yuan, H.L., Liu, X.M., Liu, Y.S., Xu, W.L., Ling, W.L., Ayers, J., Wang, X.C., Wang, Q.H., 2004. Recycling lower continental crust in the North China craton. Nature 432, 892–897.

Garland, F., Turner, S., Hawkesworth, C.J., 1996. Shifts in the source of the Parana basalts through time. Lithos 37, 223–243.

Green, D.H., Ringwood, A.E., 1967. The stability fields of aluminous pyroxene peridotite and garnet peridotite and their relevance in upper mantle structure. Earth Planet. Sci. Lett. 3, 151–160.

Griffin, W.L., O'Reilly, S.Y., Ryan, C.G., 1992. Composition and thermal structure of the lithosphere beneath south Africa, Siberia and China: proton microprobe studies. Abstract of International Symposium on Cenozoic Volcanic Rocks and Deep-seated Xenoliths of China and its Environs. Beijing, pp. 65–66.

Griffin, W.L., Zhang, A.D., O'Reilly, S.Y., Ryan, C.G., 1998. Phanerozoic evolution of the lithosphere beneath the Sino-Korean Craton. In: Flower, M.F., Chung, S.L., Lo, C.H., Lee, T.Y. (Eds.), Mantle Dynamics and Plate Interactions in East Asia. American Geophysical Union, Geodynamics Series, vol. 27, pp. 107–126.

Hart, S.R., 1984. A large-scale isotope anomaly in the Southern Hemisphere mantle. Nature 309, 753–757.

Hauser, E., Potter, C., Hauge, T., Burgess, S., Burtch, S., Mutschler, R., Allmendinger, R., Brown, L., Kaufman, S., Olivier, J., 1987.

Crustal structure of eastern Nevada from COCORP deep seismic reflection data. Geol. Soc. Amer. Bull. 99, 833–844.
Hawkesworth, C., Gallagher, K., 1993. Mantle hotspots, plumes and regional tectonics as causes of intraplate volcanism. Terra Nova 5, 552–559.
Hawkesworth, C., Kelley, S., Turner, S., Le Roux, A., Storey, B., 1999. Mantle processes during Gondwana break-up and dispersal. J. Afr. Earth Sci. 28, 239–261.
Hendrie, D.B., Kusznir, N.J., Morley, C.K., Ebinger, C.J., 1994. Cenozoic extension in northern Kenya: a quantitative model of rift basin development in the Turkana region. Tectonophysics 236, 409–438.
Hergt, J.M., Peate, D.W., Hawkesworth, C.J., 1991. The petrogenesis of Mesozoic Gondwana low-Ti flood basalts. Earth Planet. Sci. Lett. 105, 134–148.
Hoffmann, A.W., 1997. Mantle geochemistry: the message from oceanic volcanism. Nature 385, 219–228.
Hofmann, A.W., Jochum, K.P., Seufert, M., White, W.M., 1986. Nb and Pb in oceanic basalts: new constraints on mantle evolution. Earth Planet. Sci. Lett. 79, 33–45.
Hollanda, M.H., Pimentel, M.M., Oliveira, D.C., Jardim de Sa, E.F., 2006. Lithosphere–asthenosphere interaction and the origin of Cretaceous tholeiitic magmatism in Northeastern Brazil: Sr–Nd–Pb isotopic evidence. Lithos 86, 34–49.
Isozaki, Y., 1997. Jurassic accretion tectonics of Japan. Isl. Arc 6, 25–51.
Jahn, B.M., Wu, F.Y., Lo, C.H., Tsai, C.H., 1999. Crust–mantl e interaction induced by deep subduction of the continental crust: geochemical and Sr–Nd isotopic evidence from post-collisional mafic–ultramafic intrusions of the northern Dabie complex, central China. Chem. Geol. 157, 119–146.
Jiang, N., 2005. Petrology and geochemistry of the Shuiquangou syenitic complex, northern margin of the North China Craton. J. Geol. Soc. (Lond.) 162, 203–215.
Jin, J., Meng, Q.R., Zhang, Y., Xu, D., 2000. Jurassic–Cretaceous evolution of the Yingen basin and its petroleum potential. Acta Petrol. Sin. 21, 13–19 (in Chinese with English abstract).
Karson, J.A., Curtis, P.C., 1989. Tectonic and magmatic processes in the eastern branch of the East African Rift and implications for magmatically active continental rifts. J. Afr. Earth Sci. 8, 431–453.
Klemme, S., O'Neill, H.StC., 2000. The near-solidus transition from garnet lherzolite to spinel lherzolite. Contrib. Mineral. Petrol. 138, 237–248.
Li, X.H., Liu, Y., Tu, X.L., Hu, G.Q., Zeng, W., 2002. Precise determination of chemical compositions in silicate rocks using ICP-AES and ICP-MS: a comparative study of sample digestion techniques of alkali fusion and acid dissolution. Geochimica 31, 289–294 (in Chinese with English abstract).
Lightfoot, P.C., Hawkesworth, C.J., Hergt, J., Naldrett, A.J., Gorbatchev, N.S., Fedorenko, V.A., Doherty, W., 1993. Remobilisation of the continental lithosphere by a mantle plume: major-, trace-element, and Sr-, Nd-, and Pb-isotope evidence from picritic and tholeiitic lavas of the Noril'sk District, Siberian Traps, Russia. Contrib. Mineral. Petrol. 114, 171–188.
Liu, C.Q., Xie, G.H., Masuda, A., 1996. REE, Sr and Nd isotope geochemistry of mantle xenoliths from basalts in Hannuoba. Acta Petrol. Sin. 12, 382–389.
Liu, Y.S., Gao, S., Jin, S.Y., Hu, S.H., Sun, M., Zhao, Z.B., Feng, J.L., 2001. Geochemistry of lower crustal xenoliths from Neogene Hannuoba Basalt, North China Craton: implications for petrogenesis and lower crustal composition. Geochim. Cosmochim. Acta 65, 2589–2604.
Liu, Y.S., Yuan, H.L., Gao, S., Hu, Z.C., Wang, X.C., Liu, X.M., Ling, W.L., 2004a. Zircon U–Pb ages of olivine pyroxenite xenoliths from Hannouba: genetic relation between magmatic underplating and granulite metamorphism during 95–158 Ma. Chin. Sci. Bull. 49, 790–797.
Liu, Y.S., Gao, S., Yuan, H.L., Zhou, L., Liu, X.M., Wang, X.C., Hu, Z.C., Wang, L.S., 2004b. U–Pb zircon ages and Nd, Sr, and Pb isotopes of lower crustal xenoliths from North China Craton: insights on evolution of lower continental crust. Chem. Geol. 211, 87–109.
Lu, F.X., Zheng, J.P., Wang, F.Z., Sun, P., Liu, Y.S., Zhao, L., 1997. The comparison of constitution and thermal condition in North China Craton, Yangtze Craton and Qnling orogenic belt. Earth Sci. J. Chin. Univ. Geosci. 22, 247–251 (in Chinese with English Abstract).
Lu, F.X., Zheng, J.P., Li, W.P., Chen, M.H., Chen, Z.M., 2000. The mantle evolution pattern of Phanerozoic mantle in the eastern China: the "Mushroom Cloud" model. Geosci. Front. 7, 97–107 (in Chinese with English Abstract).
Lustrino, M., 2005. How the delamination and detachment of lower crust can influence basaltic magmatism. Earth-Sci. Rev. 72, 21–38.
MacCready, T., Snoke, A.W., Wright, J.E., Howard, K., 1997. Mid-crustal flow during Tertiary extension in the Ruby Mountains core complex, Nevada. Geol. Soc. Amer. Bull. 109, 1576–1594.
McDonough, W.F., 1990. Constraints on the composition of the continental lithospheric mantle. Earth Planet. Sci. Lett. 101, 1–18.
McKenzie, D., 1985. The extraction of magma from the crust and mantle. Earth Planet. Sci. Lett. 74, 81–91.
Mechie, J., Keller, G.R., Prodehl, C., Gaciri, S., Braile, L.W., Mooney, W.D., Gajewski, D., Sandmeier, K.-J., 1994. Crustal structure beneath the Kenya Rift from axial profile data. Tectonophysics 236, 179–199.
Meng, Q.R., 2003. What drove late Mesozoic extension of the northern China–Mongolia tract? Tectonophysics 369, 155–174.
Menzies, M.A., Xu, Y.G., 1998. Geodynamics of the North China Craton. In: Flower, M.F., Chung, S.L., Lo, C.H., Lee, T.Y. (Eds.), Mantle Dynamics and Plate Interactions in East Asia. American Geophysical Union, Geodynamics Series, vol. 27, pp. 155–165.
Menzies, A., Fan, W.M., Zhang, M., 1993. Paleozoic and Cenozoic lithoprobes and the loss of >120 km of Archean lithosphere, Sino-Korean craton, China. In: Prichard, H.M., et al. (Eds.), Magmatic processes and plate tectonics. Geol. Soc. London, Special Publication, vol. 76, pp. 71–81.
Modeland, S., Francis, D., Hynes, A., 2003. Enriched mantle components in Proterozoic continental-flood basalts of the Cape Smith foldbelt, northern Quebec. Lithos 71, 1–17.
Morris, G.A., Larson, P.B., Hooper, P.R., 2000. "Subduction style" magmatism in a non-subduction setting: the Colville igneous complex, NE Washington State, USA. J. Petrol. 41, 43–67.
O'Brien, H.E., Irving, A.J., McCallum, I.S., Thirlwall, M.F., 1995. Strontium, neodymium, and lead isotopic evidence for the interaction of post-subduction asthenospheric potassic mafic magmas of the Highwood Mountains, Montana, USA, with ancient Wyoming craton lithospheric mantle. Geochim. Cosmochim. Acta 59, 4539–4556.
O'Reilly, S.Y., Griffin, W.L., Poudjom Djomani, Y.H., Morgan, P., 2001. Are lithospheres forever? Tracking changes in sub-continental lithospheric mantle through time. GSA Today 11 (4), 4–10.
Parsons, T., 1995. The Basin and Range Province. In: Olsen, K.H. (Ed.), Continental Rifts: Evolution, Structure, Tectonics. Developments in Geotectonics, vol. 25, pp. 277–324.

Pearce, J.A., Thirlwall, M.F., Ingram, G., Murton, B.J., Arculus, R.J., Van der Laan, S.R., 1992. Isotopic evidence for the origin of Boninites and related rocks drilled in the Izu-Bonin (Ogasawara) forearc, Leg 125. In: Fryer, P., Pearce, J.A., Stokking, L. (Eds.), Proceedings of the Ocean Drilling Program. Scientific Results, vol. 125, pp. 237–261.

Ritts, B.D., Darby, B.J., Cope, T., 2001. Early Jurassic extensional basin formation in the Daqing Shan segment of the Yinshan belt, northern North China, Inner Mongolia. Tectonophysics 339, 239–258.

Robinson, J.A., Wood, B.J., 1998. The depth of the spinel to garnet transition at the peridotite solidus. Earth Planet. Sci. Lett. 164, 277–284.

Rollinson, H.R., 1995. Using geochemical data: evaluation, presentation, interpretation. British Library Cataloguing-in-Publication Data. Longman, p. 352.

Rudnick, R.L., Fountain, D.M., 1995. Nature and composition of the continental crust: a lower crustal perspective. Rev. Geophys. 33, 267–309.

Rudnick, R.L., Prespcr, T., 1990. Geochemistry of intermediate- to high-pressure granulites. In: Vielzeuf, D., Vidal, Ph. (Eds.), Granulites and Crustal Evolution. Kluwer, Dordrecht, pp. 523–550.

Rudnick, R.L., McDonough, W.F., McCulloch, M.T., Taylor, S.R., 1986. Lower crustal xenoliths from Queensland, Australia: evidence for deep crustal assimilation and fractionation of continental basalts. Geochim. Cosmochim. Acta 50, 1099–1115.

Rudnick, R.L., Gao, S., Ling, W.L., Liu, Y.S., McDonough, W.F., 2004. Petrology and geochemistry of spinel peridotite xenoliths from Hannuoba and Qixia, North China craton. Lithos 77, 609–637.

Ruppel, C., 1995. Extensional processes in continental lithosphere. J. Geophys. Res. 100, 24187–24215.

Shao, J.A., Mou, B.L., He, G.Q., Zhang, L.Q., 1997. Geological evolution in the northern margin of the North China Craton in the superposed process of the Paleo-Asian and Paleo-Pacific realms. Sci. China. Ser. D 27, 390–394.

Shaw, J.E., Baker, J.A., Menzies, M.A., Thirlwall, M.F., Ibrahim, K.M., 2003. Petrogenesis of the largest intraplate volcanic field on the Arabian plate (Jordan): a mixing lithosphere–asthenosphere source activated by lithospheric extension. J. Petrol. 44, 1657–1679.

Song, Y., Frey, F.A., 1989. Geochemistry of peridotite xenoliths in basalt from Hannuoba, Eastern China: implications for subcontinental mantle heterogeneity. Geochim. Cosmochim. Acta 53, 97–113.

Song, Y., Frey, F.A., Zhi, X., 1990. Isotopic characteristics of Hannuoba basalts, eastern China: implications for their petrogenesis and the composition of subcontinental mantle. Chem. Geol. 85, 35–52.

Stewart, K., Rogers, N.W., 1996. Mantle plume and lithosphere contributions to basalts from southern Ethiopia. Earth Planet. Sci. Lett. 139, 195–211.

Sun, S.S., McDonough, W.F., 1989. Chemical and isotopic systematics of oceanic basalts: implications for mantle composition and processes. In: Saunders, A.D., Norry, M.J. (Eds.), Magmatism in the Ocean Basins. Geol. Soc. Special Pub., pp. 313–345.

Sun, Y.W., Liu, P.J., Feng, J., 1996. Early Jurassic fossil plants from the Nandaling Formation in the vicinity of Shanggu, Chengde of Hebei. J. Changchun Univ. Earth Sci. 26, 9–16 (in Chinese with English abstract).

Tatsumoto, M., Basu, A.R., Huang, W., Wang, J., Xie, G., 1992. Sr, Nd, and Pb isotopes of ultramafic xenoliths in volcanic rocks of eastern China: enriched components EMI and EMII in subcontinental lithosphere. Earth Planet. Sci. Lett. 113, 107–128.

Wang, K., Plank, T., Walker, J.D., Smith, E.I., 2002. A mantle melting profile across the Basin and Range, SW USA. J. Geophys. Res. 107. doi:10.1029/2001JB000209.

Wilde, S.A., Zhou, X.H., Nemchin, A.A., Sun, M., 2003. Mesozoic crust–mantle interaction beneath the North China Craton: a consequence of the dispersal of Gondwanaland and accretion of Asia. Geology 31, 817–820.

Xu, Y.G., 2001. Thermo-tectonic destruction of the Archean lithospheric keel beneath the Sino-Korean Craton in China: evidence, timing and mechanism. Phys. Chem. Earth, Part A Solid Earth Geod. 26, 747–757.

Yan, G.H., Mou, B.L., Xu, G.L., He, G.Q., Tang, L.K., Zhao, H., He, Z.P., Zhang, R.H., Qiao, G.S., 2000. Geochronology and Sr, Nd, and Pb isotopes of the Triassic alkaline intrusions in the Yanliao–Yinshan belt, and their implications. Sci. China 30, 384–387.

Yin, A., Nie, S., 1996. A Phanerozoic palinspastic reconstruction of China and its neighboring regions. In: Yin, A., Harrison, T.M. (Eds.), Tectonic Evolution of Asia. Cambridge Univ Press, Cambridge, pp. 442–485.

Yuan, X.C., 1996. Velocity structure of the Qinling lithosphere and mushroom cloud model. Sci. China. Ser. D 39, 235–244.

Zhai, M.G., Zhu, R.X., Liu, J.M., Meng, Q.R., Hou, Q.L., Hu, S.B., Lu, W., Li, Z., Zhang, H.F., 2004. Time range of Mesozoic tectonic regime inversion in eastern North China Block. Sci. China. Ser. D 47, 151–159.

Zhang, H.F., Sun, M., Zhou, X.H., Fan, W.M., Zhai, M.G., Yin, J.F., 2002. Mesozoic lithosphere destruction beneath the North China Craton: evidence from major, trace element, and Sr–Nd–Pb isotope studies of Fangcheng basalts. Contrib. Mineral. Petrol. 144, 241–253.

Zhang, H.F., Sun, M., Zhou, X.H., Zhou, M.F., Fan, W.M., Zheng, J.P., 2003. Secular evolution of the lithosphere beneath the eastern North China Craton: evidence from Mesozoic basalts and high-Mg andesites. Geochim. Cosmochim. Acta 67, 4373–4387.

Zhang, H.F., Sun, M., Zhou, M.F., Fan, W.M., Zhou, X.H.M.G., 2004. Highly heterogeneous Late Mesozoic lithospheric mantle beneath the North China Craton: evidence from Sr–Nd–Pb isotopic systematics of mafic igneous rocks. Geol. Mag. 141, 55–62.

Zhao, Y., Yang, Z.Y., Ma, X.H., 1994. An important transition in the development of east Asian tectonics. Chin. J. Geol. 29, 105–119 (in Chinese with English abstract).

Zhao, Y., Cui, S.Q., Guo, T., Xu, G., 2002. Evolution of a Jurassic basin of the Western Hills, Beijing, north China and its tectonic implications. Geol. Bull. China 21, 211–217 (in Chinese with English abstract).

Zheng, J.P., Lu, F.X., 1999. Petrologic characteristics of kimberlite-borne mantle xenoliths from the Shandong and Liaoning Peninsula: Paleozoic lithosphere mantle and its heterogeneity. Acta Petrol. Sin. 15 (1), 65–74 (in Chinese with English abstract).

Zheng, J.P., O'Reilly, S.Y., Griffin, W.L., Lu, F.X., Zhang, M., Pearson, N.J., 2001. Relict refractory mantle beneath the eastern North China block: significance for lithosphere evolution. Lithos 57, 43–66.

Zheng, Y.D., Davis, G.A., Wang, C., Darby, B.J., Zhang, C.H., 2000. Major Mesozoic tectonic events in the Yanshan belt and the plate tectonic setting. Acta Geol. Sin. 74, 289–302 (in Chinese with English abstract).

Zhi, X., Song, Y., Frey, F.A., Feng, J., Zhai, M., 1990. Geochemistry of Hannuoba basalts, eastern China: constraints on the origin of

continental alkaline and theoleiitic basalt. Chem. Geol. 88, 1–33.

Zhou, X.H., Sun, M., Zhang, G.H., Chen, S.H., 2002. Continental crust and lithospheric mantle interaction beneath North China: isotopic evidence from granulite xenoliths in Hannuoba, Sino-Korean craton. Lithos 62, 111–124.

Zorin, Y.A., 1999. Geodynamics of the western part of the Mongolia–Okhotsk collisional belt, Trans-Baikal region (Russia) and Mongolia. Tectonophysics 306, 33–56.

Zou, H.B., Zindler, A., 1996. Constraints on the degree of dynamic partial melting and source composition using concentration ratios in magmas. Geochim. Cosmochim. Acta 60, 711–717.

Zou, H.B., Zindler, A., Xu, X.S., Qi, Q., 2000. Major, trace element, and Nd, Sr and Pb isotope studies of Cenozoic basalts in SE China: mantle sources, regional variations and tectonic significance. Chem. Geol. 171, 33–47.

Zou, H.B., Reid, M.R., Liu, Y.S., Yao, Y.P., Xu, X.S., Fan, Q.C., 2003. Constraints on the origin of historic potassic basalts from northeast China by U–Th disequilibrium data. Chem. Geol. 200, 189–201.